Wear 599 (2026) 206758

Contents lists available at ScienceDirect

Wear

journal homepage: www.elsevier.com/locate/wear

Tribo-acoustic informatics of FDM printed PLA surfaces under dry sliding: The coupled influence of printing parameters and surface structures

Kunbo Lei [a], Feiyang He [b], Muhammad Khan [b,*]

[a] Nanjing University of Aeronautics and Astronautics, Nanjing, 210000, China
[b] Cranfield University, Cranfield, MK43 0AL, UK

ARTICLE INFO

Keywords:
Fused deposition modeling (FDM)
Polylactic acid (PLA)
Friction-induced noise
Response surface methodology
Surface texture
3D-printing parameters

ABSTRACT

Fused deposition modelling (FDM) produces polymer surfaces whose layer-wise morphology, together with printing parameters, modulates frictional contact and tribo-acoustic emissions. This paper develops a data-driven tribo-acoustic workflow for FDM printed PLA under dry sliding and derives predictive rules for low-noise surface design within the tested process domain. Across five surface types, Plain, Triangle, Hexagonal, Straight Brush, and Curve Brush, the coefficient of friction (CoF) spanned 0.13 to 0.22 and the RMS sound pressure spanned 4.31 to 13.65 Pa. Analysis of variance shows that layer thickness is the dominant factor for both CoF and RMS noise, while printing speed is marginal for CoF and extrusion width is weak. Contrary to common intuition, periodic surface textures do not guarantee noise reduction and can amplify tonal components under unfavourable parameter combinations. Quadratic response surface models achieved R-squared values of 0.826 for coefficient of friction and 0.932 for RMS sound pressure, and validation tests yielded average prediction errors of 7.40% and 7.43%, confirming sub 10% accuracy in practice. Taguchi signal-to-noise ratio analysis for the Plain surface identifies an optimal parameter set for minimising friction and noise, with a layer thickness of 0.2 mm, a printing speed of 40 mm per second, and an extrusion width of 0.6 mm. The curated dataset and predictive models provide a basis for tribo-informatics-oriented optimisation of process settings to mitigate friction induced noise in additively manufactured polymer interfaces.

1. Introduction

Friction-induced vibration and the resulting noise are common challenges in mechanical systems such as brakes [1], gears [2], and bearings [3]. These phenomena not only affect user experience but also contribute to reduced system performance, decreased operational stability, and potential system failure. Conventional approaches to mitigating friction-induced vibration and noise have primarily focused on material selection and lubrication enhancement [4]. However, advances in additive manufacturing technologies, particularly 3D printing, have offered new opportunities for controlling such issues through the optimized design of surface structures and textures. Compared to traditional manufacturing methods, AM offers greater flexibility in fabricating complex geometries in a single step [5]. Furthermore, the ability to adjust and optimize printing parameters enables precise tuning of surface morphology, thereby facilitating the control of vibration and noise arising from frictional interactions. Despite these capabilities, research investigating the tribo-acoustic performance of 3D-printed polymers remains underdeveloped [6,7].

At the theoretical level, several studies have explained the relationship among friction, vibration, and noise. Tian et al. [8] developed a model integrating RMS sound pressure with evolving surface roughness, showing how tribological events manifest in noise emissions. Papandrea et al. [9] demonstrated that surface roughness amplitude correlates strongly with sound pressure level (SPL) under dry contact. Akay [10] and Pandey et al. [11] showed that frictional instabilities trigger squeal via mode excitation, while Zhang et al. [12] confirmed that non-linear mode coupling and sliding speed affect friction noise, linking contact dynamics, friction variability, and asperity deformation to acoustic emissions. Harisubramanyabalaji et al. [13] proposed a machine learning framework that predicts surface wear patterns based on acoustic signal descriptors. The findings suggest a clear relationship between frictional noise and the surface's tribological behavior, where enhanced tribological characteristics play a key role in suppressing noise

This article is part of a special issue entitled: Informatics of Wear_invited-only published in Wear.

* Corresponding author.
E-mail address: muhammad.a.khan@cranfield.ac.uk (M. Khan).

https://doi.org/10.1016/j.wear.2026.206758
Received 7 January 2026; Received in revised form 3 April 2026; Accepted 21 April 2026
Available online 14 May 2026
0043-1648/© 2026 The Authors. Published by Elsevier B.V. This is an open access article under the CC BY license (http://creativecommons.org/licenses/by/4.0/).

caused by sliding contact.

A wide range of research has explored how variations in 3D printing parameters influence the tribological properties of polymer materials. Hanon et al. [14] demonstrated that the friction coefficient of PLA materials is affected by build orientation and filament colour. Mitaľ et al. [15] highlighted the wear resistance benefits of alternating fibre directions in PEI, while He et al. [16]developed predictive models that integrate build angle, layer height, and lubrication state to assess wear and friction. Portoacă et al. [17] found optimal friction and wear performance for ABS and PLA at specific combinations of infill density and layer thickness. According to the findings of Mourya et al. [18], both layer height and nozzle temperature have a pronounced effect on the wear performance of 3D-printed polymers, with distinct optimal settings identified for ABS and PLA. For ABS, minimal wear was observed under a 0.1 mm layer height, a nozzle temperature of 230 °C, a line width of 0.28 mm, and a print speed of 75 mm/s. In comparison, PLA exhibited the best tribological behavior when printed at a 0.14 mm layer height, a nozzle temperature of 220 °C, a line width of 0.31 mm, and a speed of 50 mm/s. Mahmood et al. [19] reported that printing orientation relative to sliding direction induces anisotropy in wear behaviour, with PLA outperforming ABS. Hossain et al. [20] observed that higher infill densities and specific patterns improve TPU's wear resistance. Prajapati et al. [21] demonstrated that increased layer thickness in PEEK leads to higher friction and wear due to changes in surface roughness and hardness. Bohun et al. [22] found that infill type and clay content jointly affect PLA composites' frictional behaviour. Pieniak et al. [23] emphasized the role of SLA printer type and post-processing on friction and hardness. Dhakal et al. [24] revealed that defect control in Fused Deposition Modelling FDM printing—linked to raster angle and printing environment—can improve tribological stability. While these studies provide valuable insight into friction and wear trends, they seldom consider acoustic emissions or vibration responses as performance metrics.

Another stream of research has emphasized surface texture and structured design as key factors influencing tribological behaviour. Some studies using laser-textured or sintered metal substrates have demonstrated the tribological advantages of structured surfaces. Holovenko et al. [25] fabricated various stainless steel patterns that yielded distinct wear profiles. Wang et al. [26] and Yin et al. [27] introduced wedge-shaped textures on AlSi10Mg and Ti6Al4V alloys, respectively, showing improved oil retention and reduced adhesive wear. Liu et al. [28] used 3D-printed scale-like structures to enhance lubrication and reduce friction and wear under low-speed, high-load conditions. Recent studies have highlighted the impact of surface structures on tribological performance. Zhao et al. [29] designed egg carton-inspired SiOC--MoS_2/GO structures with ultra-low wear at specific curvatures. Guo et al. [30] showed that wedge-shaped textures on 3D-printed titanium alloy enhanced lubrication and reduced wear. Wang et al. [31] fabricated python-inspired Al_2O_3 composites with MoS_2 films, achieving improved friction and wear resistance. Afshar-Mohajer et al. [32] employed two-photon lithography to manipulate the stiffness of micro- and nanostructures, demonstrating its influence on both frictional forces and material deformation. These works demonstrate how geometry and multiscale design significantly influence tribological outcomes in various advanced 3D-printed materials. These works indicate the emerging relevance of AM-enabled texturing, yet most of the existing analysis continues to prioritize mechanical properties over acoustic behaviour.

In addition to studies focused on metals, some research has employed polymer materials to investigate how surface structure and texture influence tribological performance. Yuan et al. [33] reported a counter-intuitive negative friction coefficient effect in bioinspired groove-textured surfaces. Luo et al. [34] and Gkougkousi et al. [35] observed that specific geometric patterns, such as squares and semi-cylinders, significantly reduce static and dynamic friction through controlled deformation and load distribution. Cheng et al. [36] and Zhang et al. [37] proposed bionic structures like fish scales and shark-skin grooves, which improved hydrodynamic lubrication and delayed boundary layer separation, particularly relevant for underwater noise reduction. Li et al. [38] proposed a kind of microstructure that has lower friction and lower ice adhesion by over 90%, improving surface tribological performance.

Some work has begun to connect surface structures with noise and vibration outcomes. Yuan et al. [39] applied biomimetic textures to steel–elastomer contacts, noting significant reductions in noise amplitude. Chen et al. [40] designed concrete surfaces with optimized texture periodicity that lowered friction-induced noise in tire–road systems. Lu et al. [41] demonstrated that structured Ni_3Al composites reduce noise through surface energy modulation, and Jolivet et al. [42] linked gear tooth topography to radiated noise levels. John et al. [43] showed that hydrodynamic grooves on steel surfaces suppress noise via enhanced film stability. In the polymer domain, Yetgin [44] studied short fibre reinforcement in PLA composites, finding improved vibration damping but without isolating surface structure effects. Prajapati et al. [45] and Wang et al. [46] explored microchannel-infused textures and observed significant SPL attenuation during sliding, though materials used were not exclusively 3D-printed.

Despite these advancements, systematic studies involving 3D-printed surface textures and their acoustic implications are rare. Peng et al. [47] found that sinusoidal and circular laser textures reduced vibration and stabilized friction, thereby lowering noise. Most experimental investigations into friction-induced noise have relied on conventional metallic systems or laser-textured components. Zhou et al. [48] used micro-pits filled with lubricants on a titanium alloy to suppress stick-slip motion. Ma et al. [49] and Gadelmoula et al. [50] linked circular patterns and composite layups to reduced high-frequency squeal. Madison et al. [51] emphasized that layered polymer architectures affect thermal gradients and surface stability, which are crucial for vibrational response. Lu et al. [52] and Zhang et al. [53] analysed acoustic patterns arising from varying roughness and sliding speed, but their approaches remained focused on metallic or hybrid systems.

Together, these studies affirm that surface characteristics, including roughness, energy dissipation, and pattern regularity, significantly influence vibration and noise generation. However, the material systems investigated are predominantly metallic, and fabrication techniques are largely non-additive. There is thus a critical gap in the literature regarding how 3D-printed polymer surfaces, whose mechanical anisotropy, interlayer bonding, and porosity differ significantly from machined counterparts, contribute to friction-induced noise and vibration behaviour. Moreover, limited research has concurrently examined how the interplay between 3D printing parameters and surface geometry influences both tribological performance and noise generation.

The objective of this research is to investigate the impact of various 3D printing parameters and customized surface textures on the frictional and acoustic performance of polymer components. In this study, a data-driven tribo-acoustic analysis framework is adopted to systematically relate process parameters to friction and acoustic responses. This framework combines designed experiments, time-series signal acquisition, data preprocessing, statistical evaluation through ANOVA, and empirical response surface modelling to establish reproducible parameter–response relationships within the tested process domain. Through a series of well-controlled friction tests paired with real-time sound monitoring, the research aims to develop a model that connects manufacturing variables and surface characteristics to both wear behavior and noise generation. The insights gained are intended to support the development of 3D-printed surfaces with improved acoustic performance for mechanical system applications.

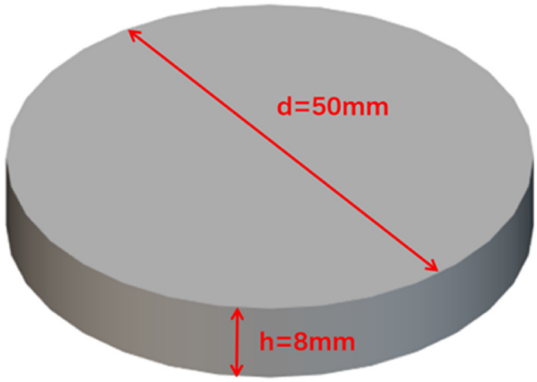


Fig. 1. Test specimen dimensions.

2. Methodology

2.1. Material and specimen preparation

All specimens were fabricated using polylactic acid (PLA) filament supplied by Ultimaker® (Geldermalsen, The Netherlands). PLA is extensively utilized in fused deposition modeling (FDM) due to its affordability, dimensional accuracy, relatively low melting temperature, and reduced tendency to warp, making it ideal for accurately replicating designed surface features.

The test specimen, depicted in Fig. 1, is a circular disc measuring 50 mm in diameter and 8 mm in thickness, conforming to the requirements of the tribological testing apparatus. The model was designed using nTopology® software and saved as an STL file, which was subsequently imported into ideaMaker® 5.2 for slicing and print parameter setup. The generated G-code was then executed by the RAISE3D Pro2® printer to fabricate the specimen. To ensure uniform print quality, all parameters except those being experimentally varied were maintained at their default settings. These included a 0.4 mm nozzle diameter, two perimeter walls, 100% line infill density, an infill speed of 60 mm/s, a 3 mm thickness for the bottom layer, a bed temperature of 60 °C, and a nozzle temperature of 205 °C.

2.2. Design of experiment (DoE)

Building on a comprehensive review of the literature, we investigated four representative surface geometries in addition to a flat control to isolate the role of topology on friction and noise. Prior studies largely fall into two themes: (i) periodic patterned arrays with prescribed geometric features and (ii) brush-like textures aimed at reducing the coefficient of friction. Accordingly, we selected two exemplars of each family—a recessed triangular circumferential array and a protruding hexagonal honeycomb, as well as straight and curved brush designs composed of cylindrical elements. The CAD definitions are shown in Fig. 2.

Besides the surface patterns shown in Fig. 2, three primary FDM printing parameters were chosen as variables for the experiment: layer thickness, surface printing speed, and extrusion width. The layer thickness denotes the vertical measurement of each deposited layer, and adjustments to this parameter influence the stepped surface texture and near-surface porosity—both of which play a critical role in frictional behavior. Surface printing speed is the nozzle travel rate when forming the outer surfaces; it affects surface finish, dimensional accuracy, and thermal history. Extrusion width is the horizontal width of each deposited filament; by governing bead overlap and inter-line bonding, it

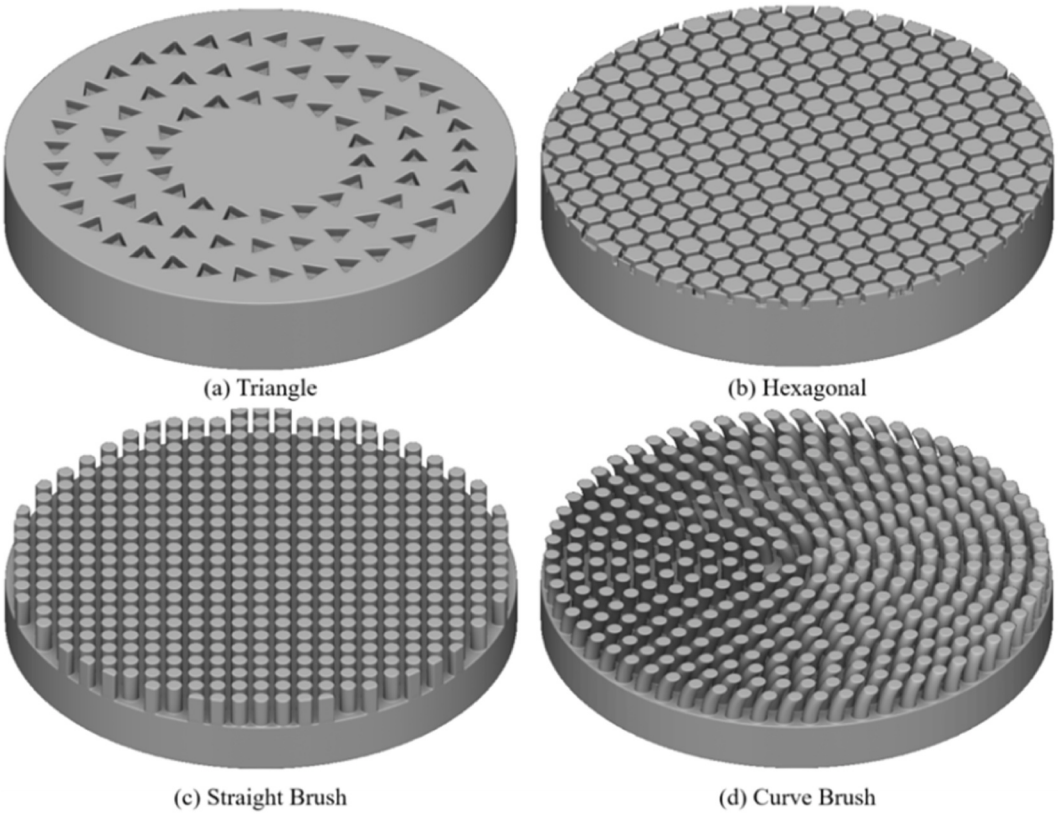


Fig. 2. Surface-structure geometries (dimensions in mm). (a) Triangle: three circumferential rings of equilateral triangular pits inscribed in 3-mm circles at radii 10, 15, and 20; depth 1. (b) Hexagonal: periodic array of regular hexagonal protrusions, side length 1.75, height 0.5, spacing 0.5. (c) Brush (straight): periodic array of cylindrical posts, diameter 1.5, height 3, spacing 2. (d) Curved brush: circumferentially oriented curved cylindrical posts generated by sweeping a 1.5-mm-diameter circle along an arc; height 3.

Table 1
Independent variables and levels used in the experiments.

Parameters	Values				
Surface Structures	Plain	Straight Brush	Curve Brush	Triangle	Hexagonal
Layer Thickness (mm)	0.1	0.2		0.3	
Printing Speed (mm/s)	20	40		60	
Extrusion Width (mm)	0.4	0.6		0.8	

impacts dimensional stability, mechanical integrity, and surface quality.

Each parameter was assigned three distinct levels as detailed in Table 1. Within ideaMaker, the "Standard" quality setting generally corresponds to a 0.2 mm layer thickness, an approximate top-surface printing speed of 30 mm/s, and an extrusion width of 0.4 mm. Accordingly, we chose 0.1/0.2/0.3 mm for layer thickness to span the default and reveal nonlinearity; 20/40/60 mm/s for surface printing speed to cover a practical operating range; and 0.4/0.6/0.8 mm for extrusion width (commonly set at or slightly above nozzle diameter) to probe inter-line bonding effects. Together with the five surface structures, these define four independent variables for the study.

A two-stage DoE was adopted to quantify effects and interactions while keeping the test matrix economical. Because the study includes one five-level geometric factor (surface structure) and three three-level process factors (layer thickness, surface printing speed, extrusion width), a single Taguchi array covering all factors is impractical. We therefore used a Taguchi L9 orthogonal array (3^3) for the three process factors and executed this L9 within each level of the geometric factor (i.e., blocked by surface structure). This yielded $5 \times 9 = 45$ distinct parameter sets; each set was tested in triplicate to ensure accuracy and reliability.

Alongside the Taguchi experimental design, a full factorial design ($3 \times 3 \times 3$) was implemented for the Plain surface to facilitate an in-depth examination of the three printing parameters and to generate ample data for modeling both the coefficient of friction (CoF) and root mean square (RMS) sound pressure. Using the previously defined levels, 27 unique combinations were printed; each was again run three times following the same protocol, and CoF and RMS sound pressure were recorded. In total, the design comprised 135 Taguchi tests (45×3) and 81 full-factorial tests (27×3). This two-stage strategy balances statistical efficiency (screening via L9) with model fidelity (dense coverage on Plain) for robust inference and predictive modelling.

2.3. Experiment setup and procedure

The tribological tests were carried out on an Anton Paar TRB3 pin-on-disc tribometer (Fig. 3), which provides controlled disc rotation and synchronized acquisition of tangential force and coefficient of friction (CoF). Before testing, all printed samples were dried in an oven. Each disc-shaped specimen was secured using a three-jaw chuck, while a stainless steel ball (223 HB hardness, 194 GPa modulus of elasticity) was fixed to the test arm and positioned perpendicular to the specimen's surface.

To improve accuracy, reduce random error, and maximize specimen utilization, three sliding radii were used for each parameter set: r = 10, 15, 20 mm. Tests were conducted under a 5 N normal load and 300 rpm disc speed for 1 min at 25 °C. These conditions produced steady sliding of the ball across the printed surface.

The TRB3 software continuously recorded F (tangential friction force) and μ (Coefficient of friction (COF)). The COF was computed from the time-averaged friction force over the analysis window used throughout this study, and then averaged over the three radii for each parameter set.

For acoustic measurements, a G.R.A.S. sound-pressure sensor was rigidly mounted to the tribometer via a custom bracket to ensure positional stability. The sensor captured airborne sound generated during sliding; signals were subsequently processed together with the force data as described in the data-reduction procedure (windowing and RMS estimation applied consistently across all runs).

2.4. Data analysis

The raw time histories of tangential force and sound pressure were

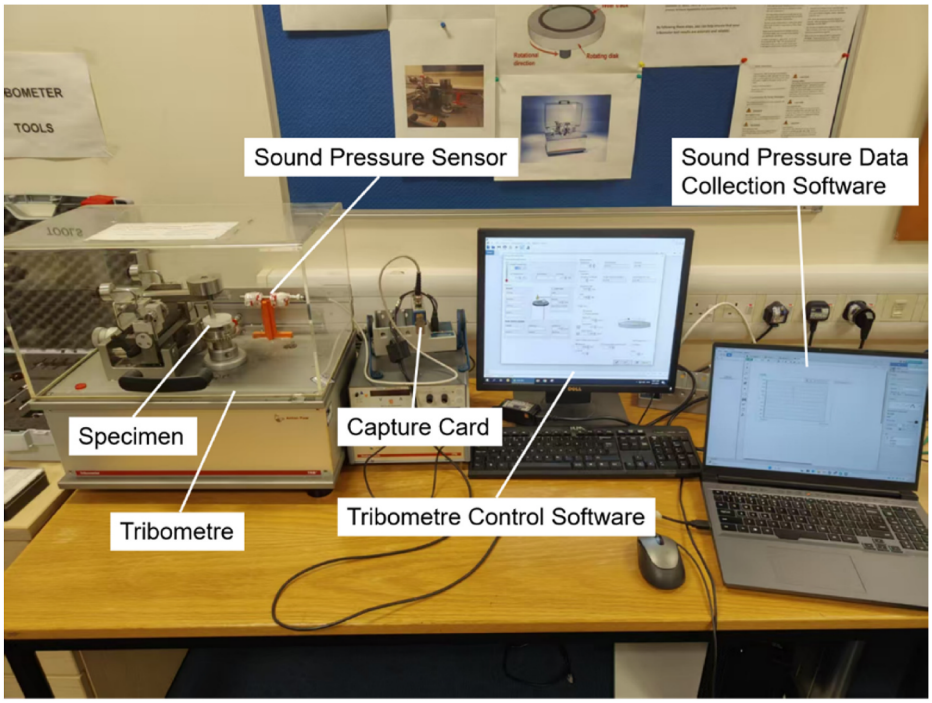


Fig. 3. Experimental setup.

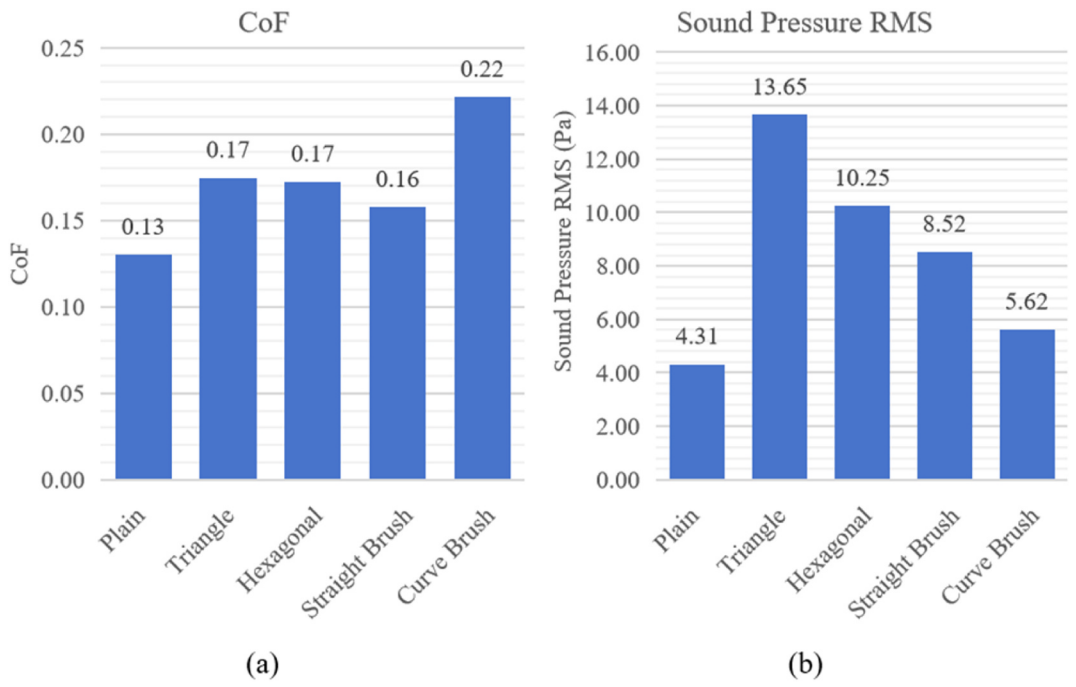


Fig. 4. Mean CoF and RMS sound pressure of different surface designs.

exported to MATLAB for post-processing. To avoid run-in and end effects, a fixed analysis window of 10–40 s after test start (30 s duration) was used for all runs.

For each parameter set, measurements were taken at three sliding radii (10, 15, 20 mm) and three repeats. Run-level results were first averaged across the repeats at each radius, and then averaged across the three radii to yield one representative COF and one RMS sound pressure per parameter set for subsequent analyses.

Because the study employs a Taguchi design, S/N ratios were used to rank factor levels with a "smaller-the-better" objective for both responses (COF and RMS). The S/N ratio for a response y with n repeats is shown in Eq. (1).

$$S/N = -10\log_{10}\left(\frac{1}{n}\sum_{i=1}^{n} y_i^2\right) \quad \text{Eq.(1)}$$

where y_i is the i-th repeated measurement. Within the Taguchi framework, larger S/N indicates a more favorable (lower) response; the level (or combination) with the highest S/N is taken as the optimum candidate. Analysis of variance (ANOVA) was employed to evaluate the statistical significance of the primary factors and their two-way interactions. The test statistic and tail probability are shown in Eq. (2) and Eq. (3).

$$F = \frac{MSB}{MSW} \quad \text{Eq.(2)}$$

$$p = P(F > F_{calculated} | df_{between}, df_{within}) \quad \text{Eq.(3)}$$

where *MSB* and *MSW* are the mean squares between and within groups, respectively, and *df* denotes the corresponding degrees of freedom. Throughout, $p < 0.05$ was regarded as statistically significant, $0.05 \leq p < 0.10$ as marginally significant, and $p \geq 0.10$ as not significant.

Quadratic response-surface models were fitted to relate the three printing parameters to COF and RMS sound pressure, respectively. Model adequacy was assessed using the coefficient of determination R^2 shown in Eq. (4) and the root-mean-square error (RMSE) shown in Eq. (5).

$$R^2 = 1 - \frac{\sum_{i=1}^{n}(y_i - \hat{y}_i)^2}{\sum_{i=1}^{n}(y_i - \bar{y})^2} \quad \text{Eq.(4)}$$

$$RMSE = \sqrt{\frac{1}{n}\sum_{i=1}^{n}(y_i - \hat{y}_i)^2} p = P(F > F_{calculated} | df_{between}, df_{within}) \quad \text{Eq.(5)}$$

where y_i are observations, $\hat{y}_i$ are model predictions, $\bar{y}$ is the sample mean, and n is the number of observations. Higher R^2 and lower RMSE indicate better predictive performance.

3. Results and discussion

3.1. Effects of surface design on noise and COF

Fig. 4 demonstrates that among the five surface types, the Plain surface showed the lowest average coefficient of friction, measured at 0.13. In contrast, the Curved Brush showed the highest COF 0.22. The remaining textures lay between these extremes, with COF values around 0.16-0.17. These results differ from trends commonly observed in metallic [26,28] or laser-textured systems [23–25,45], where periodic surface patterns typically lower friction and radiated noise. For FDM-printed polymers, however, such surface designs do not ensure quieter or smoother contact behaviour.

Regarding acoustic performance, the Plain surface recorded the lowest root mean square (RMS) sound pressure at 4.31 Pa. In contrast, the Triangle pattern produced the highest RMS value, reaching 13.65 Pa. The remaining four texture types exhibited comparable average frequencies, falling within the 32–34 Hz range. Excluding the Plain design, the Curve Brush had the next lowest RMS sound pressure at 5.62 Pa, followed by the Straight Brush at 8.52 Pa and the Hexagonal pattern at 10.25 Pa. Consistent with the coefficient of friction (CoF) trends, the four textured surfaces inspired by prior structural concepts did not achieve the anticipated noise-reduction performance.

The surface textures utilized in this work have previously been proven effective in mitigating friction-induced noise. Consequently, a reasonable explanation for this reversal lies in how textures are generated by FDM rather than in their nominal geometry. Periodic features force the nozzle to alternate deceleration, cornering and re-acceleration,

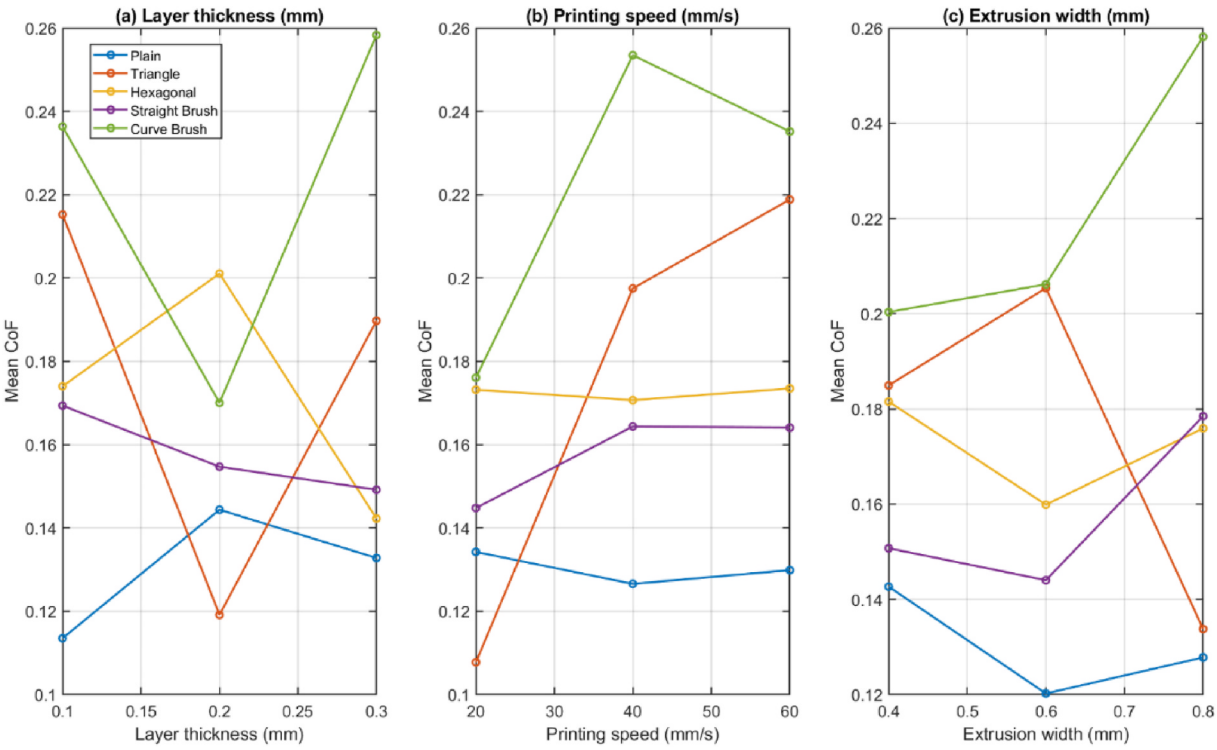


Fig. 5. Effects of printing parameters on CoF for different surface structures.

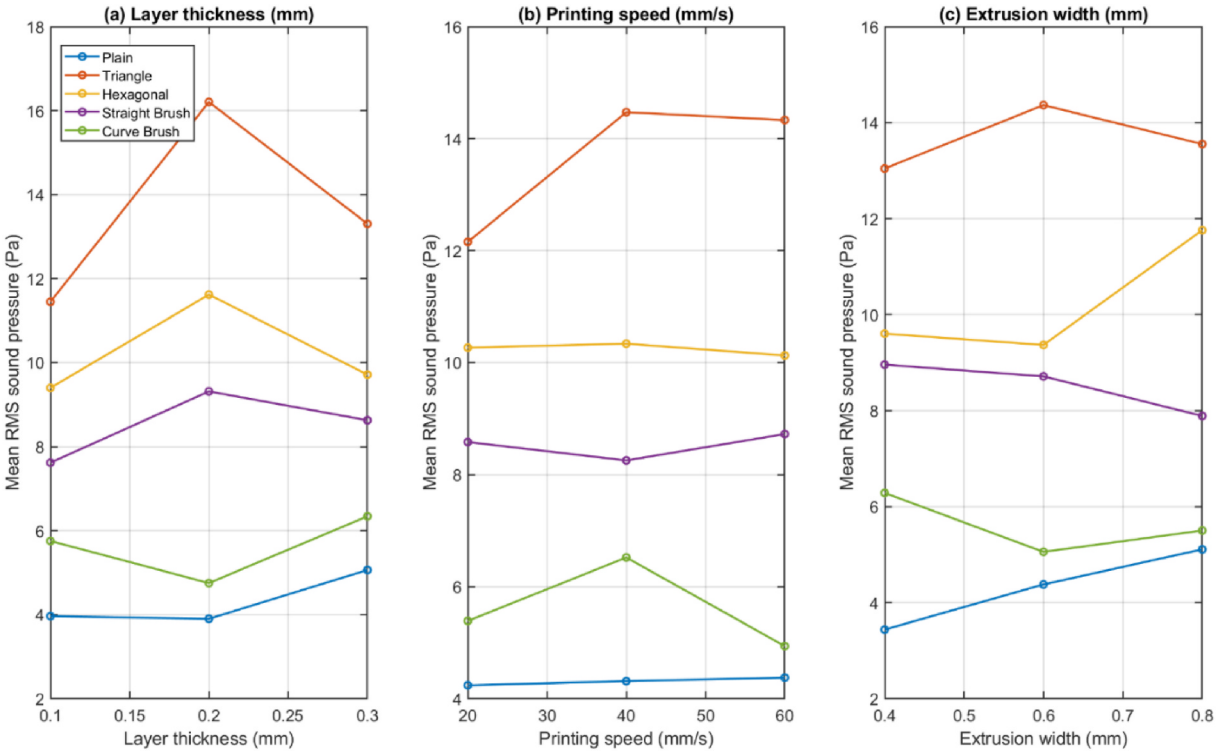


Fig. 6. Effects of printing parameters on RMS sound pressure for different surface structures.

which locally alters bead spreading and cooling, promotes material accumulation at turning points, and increases inter-track bonding heterogeneity. The resulting staircase ridges, residual waviness and near-surface porosity elevate contact roughness and tangential-force fluctuations, increasing stick–slip and amplifying radiated sound. This is most evident for geometries with sharp turns and pits such as the Triangle texture, which attains the largest RMS sound pressure. By contrast, the Plain surface avoids these path-induced defects and therefore delivers the lowest CoF and noise.

Table 2
Optimal combinations of printing parameters for each surface structure with respect to CoF.

Surface Structure	Layer Thickness	Printing Speed	Extrusion Width
Plain	0.2	40	0.6
Triangle	0.2	20	0.8
Hexagonal	0.3	40	0.6
Straight Brush	0.3	20	0.6
Curved Brush	0.2	20	0.6

Table 3
Optimal combinations of printing parameters for each surface structure with respect to sound pressure.

Surface Structure	Layer Thickness	Printing Speed	Extrusion Width
Plain	0.2	40	0.6
Triangle	0.2	20	0.8
Hexagonal	0.3	40	0.6
Straight Brush	0.3	20	0.6
Curved Brush	0.2	20	0.6

3.2. *Effects of printing parameters on acoustic responses and friction*

Figs. 5 and 6 present a summary of how the three printing parameters influence the coefficient of friction and the root mean square (RMS) sound pressure across various surface structures. Each figure presents how the measured responses vary across parameter levels for all five surface topologies. Overall, the data does not exhibit a consistent monotonic relationship between any individual printing parameter and tribological or acoustic performance. This suggests that the combined effect of material flow, inter-layer bonding, and surface geometry dominates over any single variable's contribution. In addition, the results also indicate that the mean CoF alone does not directly determine the quantitative acoustic response.

Nevertheless, several local trends are evident. Fig. 5 illustrates that the coefficient of friction for the Curved Brush texture rises with increasing extrusion width, likely due to an expanded actual contact area between the textured ridges and the mating surface as the extrusion path widens. For the Triangle structure, the slight increase in CoF with higher printing speed could be associated with thermal accumulation and partial surface smearing at elevated deposition rates. In contrast, the Straight Brush structure exhibits a modest reduction in CoF with increasing layer height, possibly due to improved contour uniformity on the top surface and smoother inter-bead transitions.

The corresponding acoustic results, depicted in Fig. 6, display similar tendencies. Most cases do not reveal a distinct linear dependence of RMS sound pressure on individual parameters, yet some structure–parameter combinations yield clear trends. The Plain surface shows increasing noise amplitude with both higher extrusion width and printing speed, consistent with the greater CoF fluctuations and stronger stick–slip modulation under those conditions. Conversely, the Straight Brush structure demonstrates a reduction in sound pressure with increasing extrusion width, suggesting that its directional ridges may stabilise the sliding contact and suppress high-frequency excitation.

Given the absence of globally consistent trends, a Taguchi signal-to-noise (S/N) analysis was employed to identify the statistically optimal combinations of printing parameters for each surface structure. The calculated S/N ratios quantify the relative sensitivity of the CoF and RMS sound pressure to parameter variations. In this framework, a higher S/N value corresponds to improved performance stability (smaller

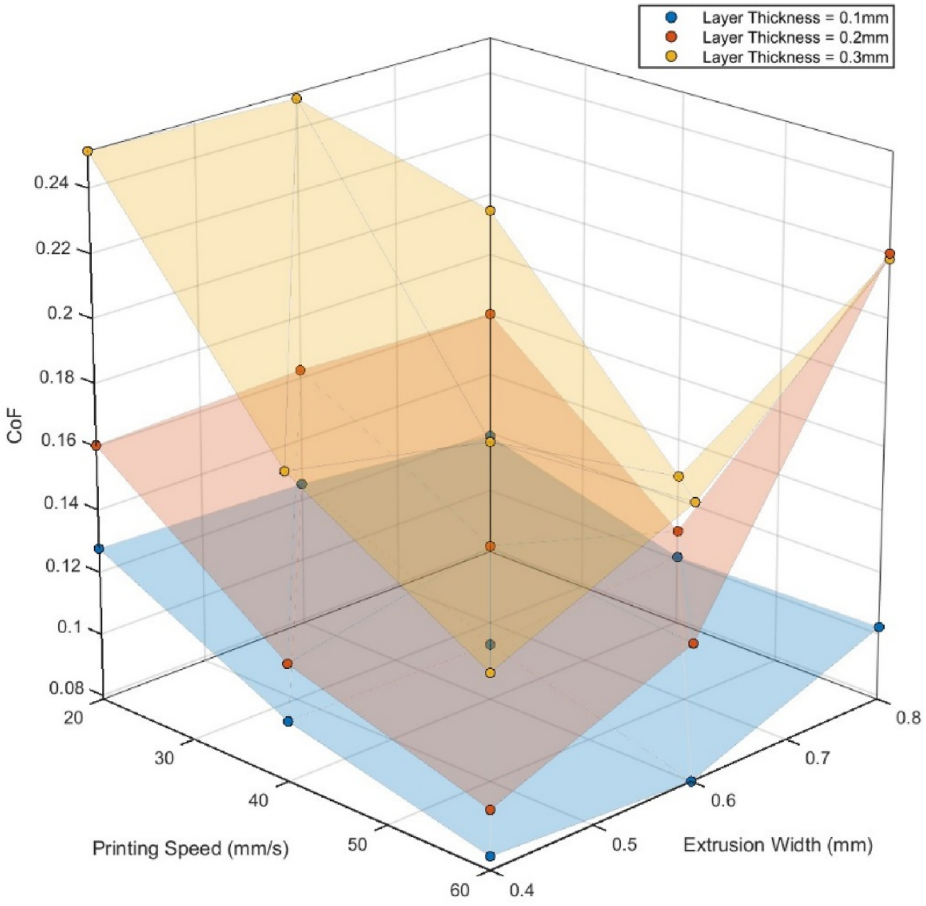


Fig. 7. Response surface of the CoF of the Plain surface as a function of printing speed and extrusion width at different layer thickness levels.

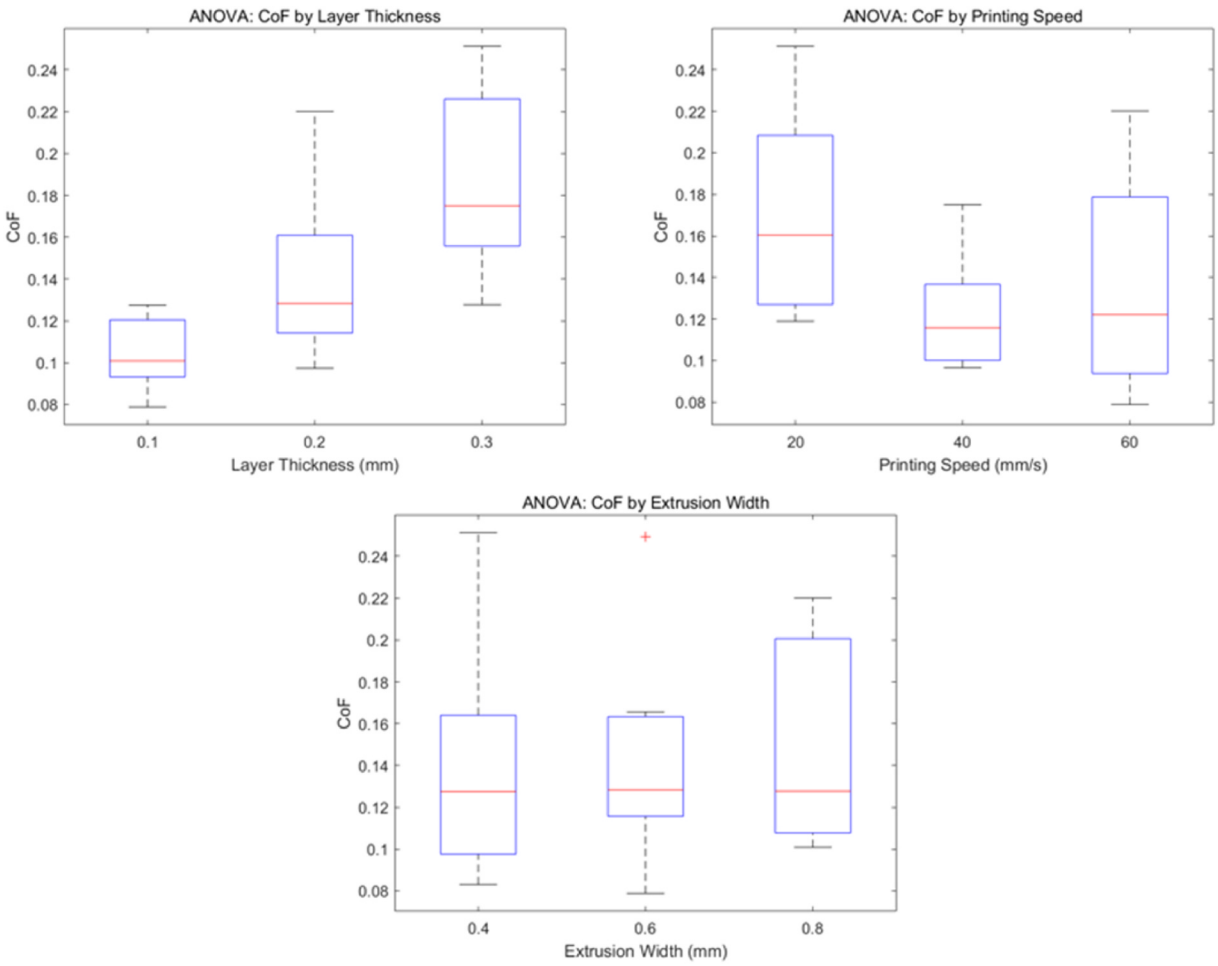


Fig. 8. ANOVA of the CoF for the Plain surface with respect to (a) layer thickness, (b) printing speed, and (c) extrusion width.

variance across trials).

The optimal parameter combinations derived from the S/N analysis are summarised in Tables 2 and 3. For both CoF and RMS sound pressure, the Plain surface achieves its best performance at moderate layer thickness (0.2 mm), high printing speed (40 mm/s), and medium extrusion width (0.6 mm). Although some structures share similar optima, others such as the Triangle and Curved Brush designs prefer narrower extrusion widths or lower speeds. Overall, the Taguchi-based evaluation confirms that while layer thickness has the most consistent influence across surface types, the synergistic effects of printing speed and extrusion width can be neglected in optimising both frictional and acoustic responses.

3.3. *Effects of printing parameters on the CoF of the plain surface*

A consistent outcome of Section 3.1 is that engineered surface textures did not confer a robust reduction in either CoF or RMS sound pressure relative to the Plain surface. This motivates a focused analysis of the Plain surface, for which a full $3 \times 3 \times 3$ factorial was executed to isolate the effects of printing parameters.

An overview of the CoF landscape across speed and extrusion width, stratified by layer thickness, is presented in Fig. 7. Each coloured plane corresponds to a different layer thickness (0.1, 0.2, and 0.3 mm). A distinct upward shift of the entire surface with increasing layer thickness demonstrates that this parameter exhibits the strongest influence on frictional behaviour. This trend is consistent with top-surface deposition mechanics in FDM.

Increasing layer thickness modifies the interlayer fusion quality and top-surface morphology in a way that directly amplifies friction. A larger layer height increases the vertical distance for heat diffusion and reduces the effectiveness of heat transfer from the newly deposited filament to the underlying layer. As a result, the previously deposited material experiences less re-melting during the subsequent pass and solidifies as a mechanically stiffer, thermally insulated layer. The weaker interlayer fusion leads to incomplete flattening of adjacent filament roads, leaving deeper inter-road valleys and more pronounced overlap ridges on the top surface. This rougher and more uneven morphology increases the local surface slope and asperity engagement during sliding, which promotes micro-ploughing and repeated formation–rupture of adhesive junctions at the contact interface, thereby elevating the average coefficient of friction. In contrast, thinner layers permit more effective interlayer heating and re-melting, leading to smoother surfaces, improved bonding, and a more stable, lower-friction contact.

By contrast, the effects of printing speed and extrusion width are far less significant. Within each layer-thickness plane, the CoF values fluctuate slightly but exhibit no clear or monotonic trend. At best, a shallow minimum appears at moderate printing speeds and medium extrusion widths, yet the changes are within the experimental scatter. The absence of consistent gradients along the speed and width axes suggests that their individual contributions to friction are secondary compared with that of layer thickness.

To quantify these observations and verify their statistical significance, an ANOVA was carried out. The corresponding boxplots in Fig. 8 show how CoF distributions vary with three printing parameters. The difference among layer thickness groups is significant, with median CoF values increasing from approximately 0.1 at 0.1 mm to 0.17 at 0.3 mm,

Table 4
p-values of the interaction terms of three parameters with respect to CoF.

Factor 1	Factor 2	p Value
Layer Thickness	Printing Speed	0.5635
Layer Thickness	Extrusion Width	0.7641
Printing Speed	Extrusion Width	0.0831

indicating a strong and consistent increased trend. By contrast, the interquartile ranges for printing speed and extrusion width overlap substantially, and their median values fluctuate within the experimental scatter. These visual observations suggest that layer thickness is the dominant factor, while the other two parameters have comparatively weak or inconsistent influences.

Quantitative ANOVA results confirm these trends. The p-value for layer thickness is 1.88×10^{-4}, well below the 0.05 significance threshold, demonstrating a statistically significant effect on CoF. Printing speed ($p = 0.0846$) is only marginally significant, and extrusion width ($p = 0.88$) has no discernible influence within the tested range. The interaction analysis summarised in Table 4 shows that none of the two-factor interactions is significant at the 0.05 level, although the combination of printing speed and extrusion width yields a marginal interaction ($p = 0.0831$). This weak coupling implies that the combined adjustment of these two parameters can occasionally modify surface morphology and frictional behaviour, even though their individual main effects remain small.

The response surface reveals a weak but distinct interaction consistent with the marginal p-value ($p = 0.0831$). At smaller extrusion widths (0.4–0.6 mm), the CoF tends to decrease slightly as printing speed increases, whereas at the largest width (0.8 mm), the trend reverses and CoF rises again beyond moderate speeds. This non-monotonic pattern indicates that frictional behaviour is governed by the interplay between material flow rate, heat transfer, and inter-track bonding during deposition.

This interaction can be rationalised in terms of the coupled thermal–geometric dynamics of filament deposition. At smaller extrusion widths, each filament carries a limited molten volume and cools rapidly upon deposition. Increasing the printing speed in this regime shortens the exposure time to elevated temperature, preventing excessive material flow and local overfilling. The deposited tracks therefore solidify with a more uniform cross-section and smaller surface waviness. Such morphological refinement reduces both the ploughing component of friction and the frequency of adhesive junction formation at the sliding interface, leading to a gradual decrease in CoF with speed. In contrast, at larger extrusion widths, the volumetric flow rate per unit time rises sharply. When the movement speed is further increased, the deposited filament retains more internal heat and the adjacent tracks have insufficient time to coalesce fully before solidification. This incomplete inter-track fusion produces microscopic voids and ridges, thereby amplifying local stress concentration and asperity interlocking during sliding. Consequently, the CoF increases again at high speed when the extrusion width is large.

3.4. *Effects of printing parameters on the acoustic response of the plain surface*

The three-dimensional response surface in Fig. 9 illustrates how the RMS sound pressure varies with printing speed and extrusion width for different layer thicknesses. A distinct upward displacement of the entire surface with increasing layer thickness confirms that this parameter has

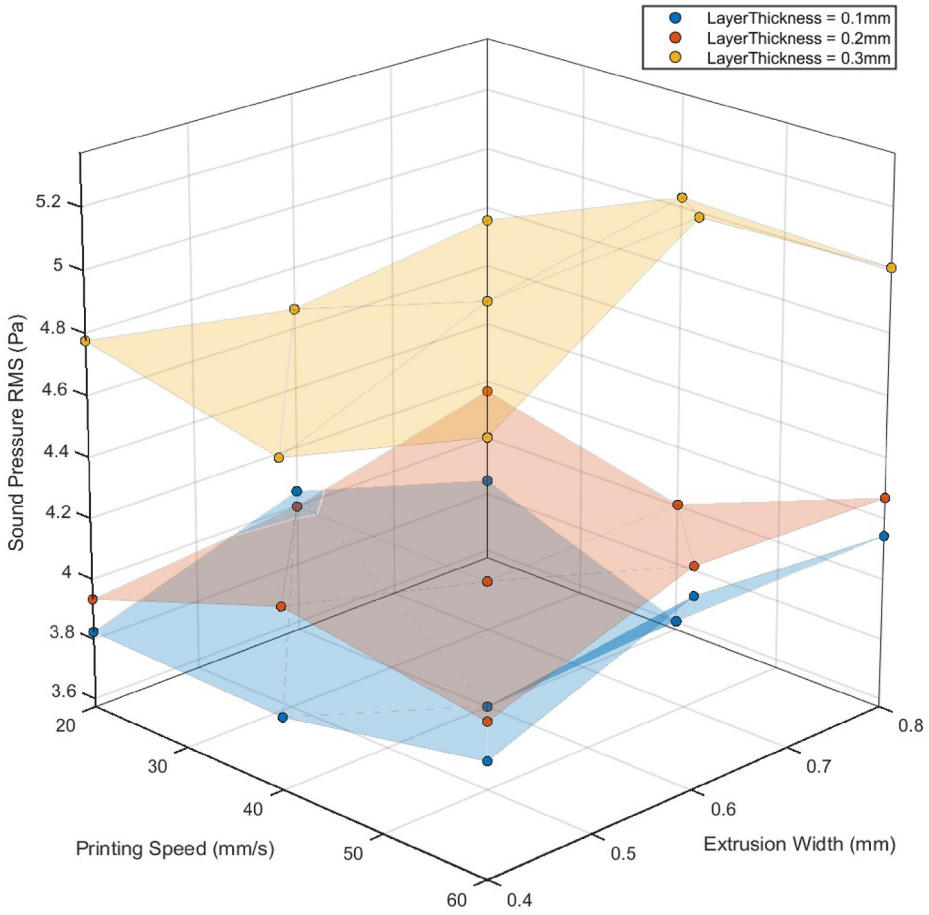


Fig. 9. Response surface of the sound pressure of the Plain surface as a function of printing speed and extrusion width at different layer thickness levels.

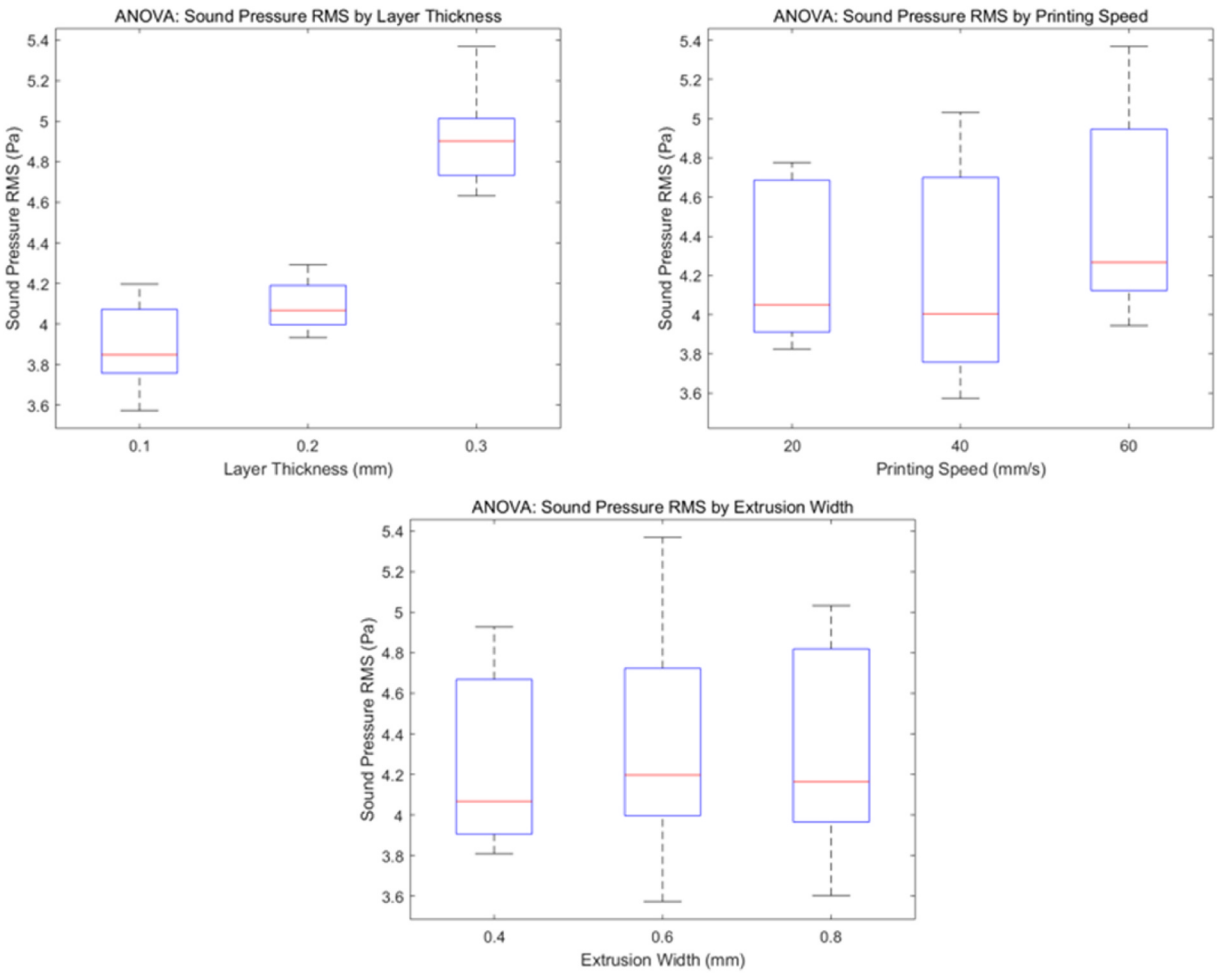


Fig. 10. ANOVA of the sound pressure for the Plain surface with respect to (a) layer thickness, (b) printing speed, and (c) extrusion width.

the most significant effect on the acoustic output, mirroring its influence on frictional behaviour. The highest RMS sound pressure, approximately 5 Pa, occurs at a layer thickness of 0.3 mm, whereas the 0.1 mm specimens consistently exhibit the lowest values around 3.8–4.0 Pa. Although friction–noise coupling is multi-physics and system-dependent, prior studies agree that fluctuations in friction force/CoF and stick–slip instabilities excite structural vibration and radiated sound [54]. The correlation between noise amplitude and friction level in our test implies that both arise from similar contact instabilities and surface–interface morphologies.

Within each layer-thickness surface, no consistent monotonic relationship is observed with either printing speed or extrusion width. For thinner layers (0.1–0.2 mm), the RMS sound pressure remains nearly constant across the parameter space, while for the thickest layer (0.3 mm) the noise slightly increases at high printing speeds and large extrusion widths. This weak dependence indicates that the acoustic response is primarily governed by the roughness and compliance of the contact interface, controlled chiefly by layer thickness, rather than by the process parameters that influence lateral bead geometry. Physically, thicker layers create a rougher, less cohesive top surface with deeper inter-road valleys and weaker interlayer bonding. These morphological irregularities promote intermittent stick–slip motion and local detachment–re-adhesion cycles during sliding, generating stronger broadband acoustic emissions. In contrast, thinner layers produce smoother and more continuous surfaces, which stabilise sliding and suppress friction-induced vibrations, thereby yielding a lower RMS sound pressure.

The statistical results obtained from ANOVA are presented in Fig. 10. The box plots clearly demonstrate that RMS sound pressure increases monotonically with layer thickness, forming three non-overlapping distributions with distinct median values. In contrast, the spreads of data for printing speed and extrusion width overlap substantially, and their medians show no consistent trend. These visual observations are confirmed quantitatively by the p-values. Layer thickness exhibits an extremely significant main effect on the acoustic response ($p = 1.02 \times 10^{-10}$), while the effects of printing speed ($p = 0.423$) and extrusion width ($p = 0.885$) are statistically insignificant. Taken together, the box plots and p-values demonstrate that the noise level is governed mainly by layer thickness, and that any variations with speed or width are comparable to experimental scatter.

Furthermore, none of the two-factor or three-factor interaction terms reaches the 95% confidence level, indicating that the acoustic emission is primarily governed by a single dominant parameter rather than complex interdependencies among the printing variables.

Table 5 reports the p-values of the pairwise interaction terms for the RMS sound pressure on the Plain surface. None of the interactions reaches statistical significance. All p-values well above 0.05 (and even 0.10), indicate that within the tested window the acoustic response does

Table 5
p-values of the interaction terms of three parameters with respect to RMS sound pressure.

Factor 1	Factor 2	p Value
Layer Thickness	Printing Speed	0.4874
Layer Thickness	Extrusion Width	0.6071
Printing Speed	Extrusion Width	0.8899

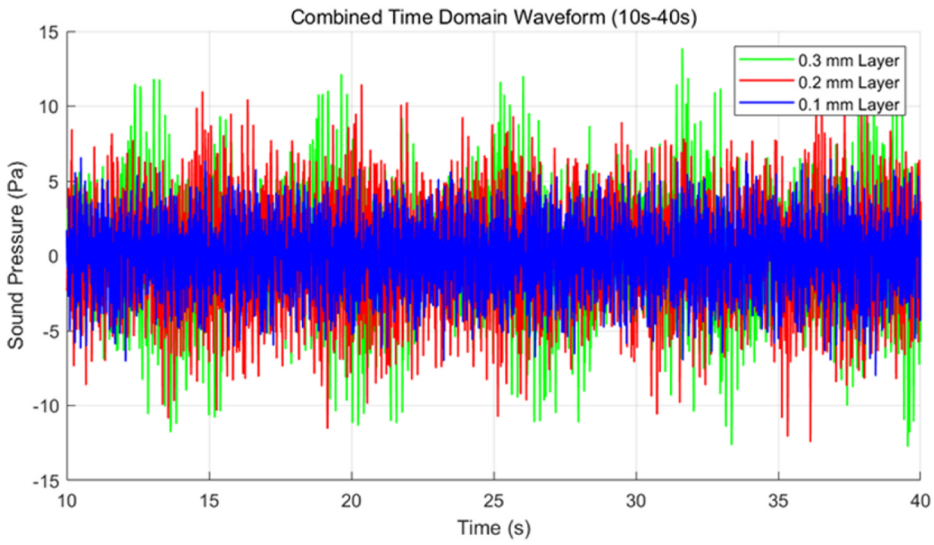


Fig. 11. Time-domain waveforms of friction noise (10–40 s) for three different layer thicknesses.

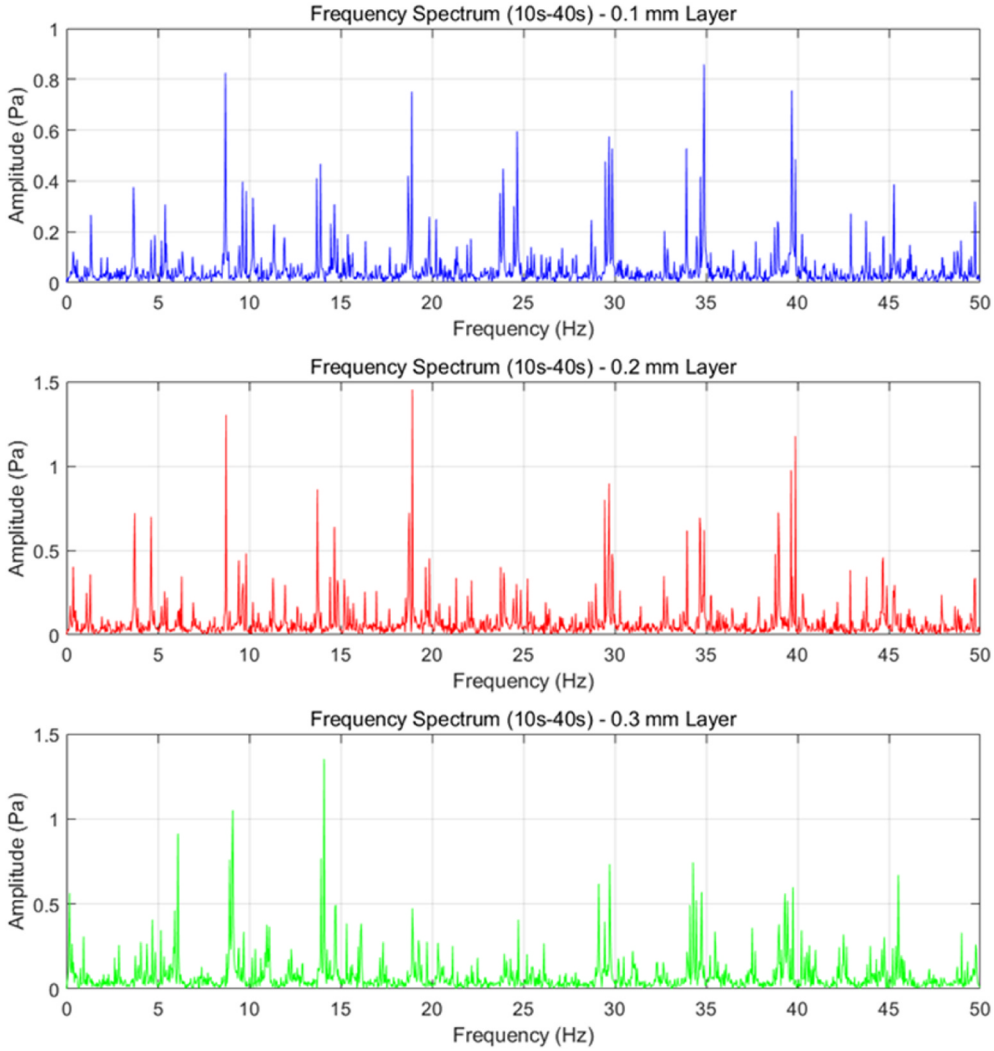


Fig. 12. FFT frequency-domain spectra for three different layer thicknesses.

not depend materially on coupled variations of the printing parameters. In other words, the rise in noise with layer thickness observed is an essentially independent effect, and adjustments to speed or extrusion width do not measurably modulate that trend through interactions.

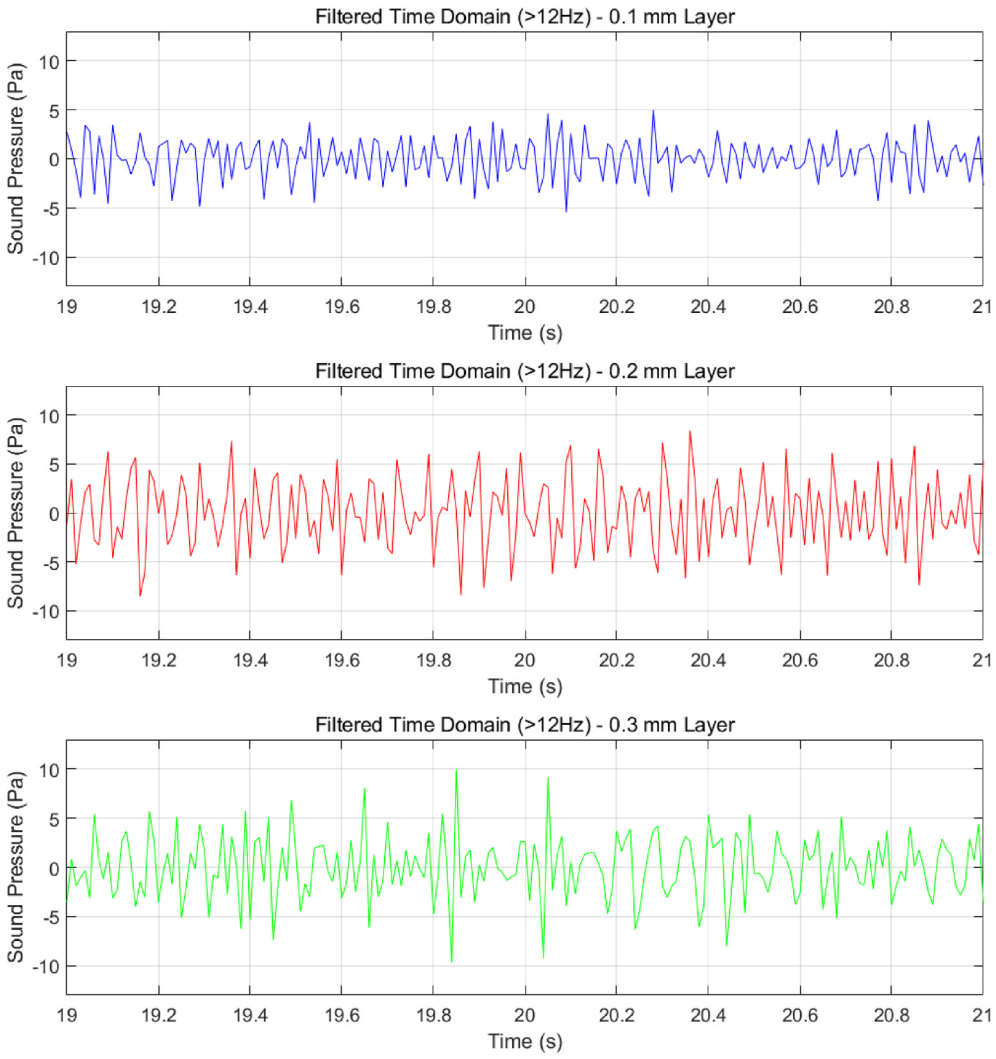


Fig. 13. Zoomed-in filtered time-domain waveforms within the 19–21 s interval.

Physically, this is consistent with the interpretation that friction-noise levels are governed by the top-surface morphology and interfacial compliance set primarily by layer height; changes in speed or width within the explored ranges do not alter these properties sufficiently to create interaction-driven changes in RMS sound pressure. This lack of interaction also justifies treating layer thickness as the dominant control variable in subsequent modelling and optimisation of the acoustic response.

3.5. *Tribo-acoustic signal analysis and mechanism interpretation*

To further reveal the physical mechanisms underlying the sharp escalation in friction noise caused by increased layer thickness, a multi-dimensional time-frequency analysis of the experimental sound pressure signals was conducted. As illustrated in Fig. 11, the time-domain sound pressure waveforms of three specimens with layer thicknesses of 0.1, 0.2, and 0.3 mm were extracted within the 10 to 40 s interval (at a constant printing speed of 20 mm/s and an extrusion width of 0.4 mm). It can be intuitively observed that as the layer thickness increases, both the overall noise baseline and the maximum transient amplitudes exhibit a significant increasing trend, which fully corroborates the reliability of the previously discussed root-mean-square (RMS) sound pressure patterns.

The frequency-domain spectra obtained by performing a Fast Fourier Transform (FFT) on the aforementioned signals are presented in Fig. 12. Since the spindle speed of the tribometer in this study was set to 300 rpm (corresponding to a fundamental mechanical excitation frequency of 5 Hz), the spectra of all three specimens exhibit response peaks at 5 Hz and its corresponding harmonics. However, their energy distributions are distinctly different. The spectrum of the 0.1 mm specimen shows low and relatively dispersed energy, indicating that its friction process is dominated by stable, continuous sliding; the weak peaks present merely represent the baseline mechanical runout noise of the equipment. In contrast, the spectrum of the 0.3 mm specimen not only exhibits an exceptionally high fundamental peak at 5 Hz but also excites prominent energy peaks at high-frequency harmonics such as 10 Hz and 15 Hz. This phenomenon, a dominant fundamental frequency accompanied by abundant high-energy harmonics, is a classical frequency-domain signature of dominant nonlinear periodic impacts (i.e., stick-slip vibrations). The spectral morphology of the 0.2 mm specimen falls between the two, representing a critical transitional state from steady-state friction to stick-slip instability.

To filter out the interference of low-frequency mechanical background noise and thus more clearly capture the true transient micro-dynamics at the contact interface, a 12 Hz high-pass filter was applied to the sound pressure data. A locally magnified time-domain waveform within a 2-s window around the 20 s mark was then extracted (Fig. 13). In the filtered plots, the 0.1 mm specimen presents an extremely flat waveform with a minimal amplitude (less than 5 Pa), confirming the absence of significant interfacial impact collisions. The 0.2 mm

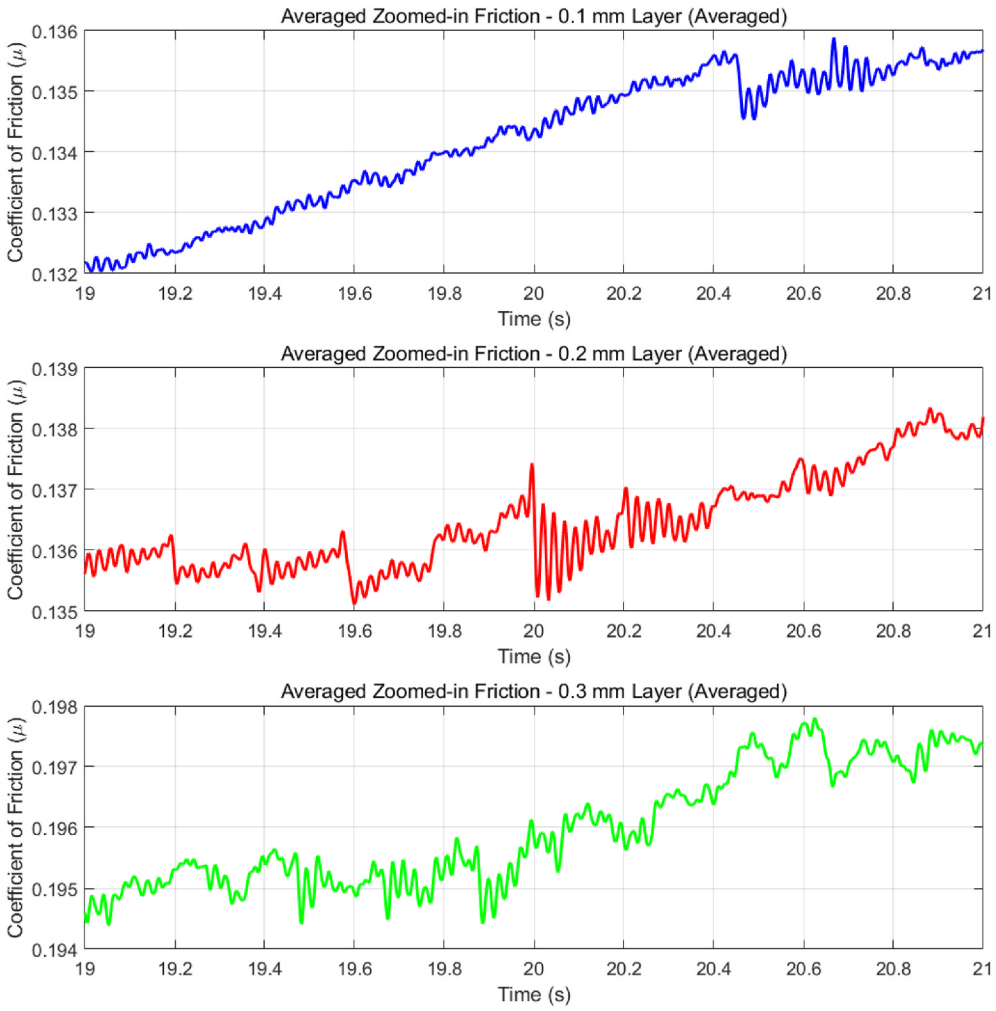


Fig. 14. Zoomed-in friction coefficient curves within the 19–21 s interval.

specimen begins to exhibit scattered, irregular pulses with amplitudes exceeding 5 Pa. Strikingly, the 0.3 mm specimen displays a highly regular, high-amplitude periodic pulse train characterized by a "flat (energy accumulation) – sudden spike (slip release) – flat" pattern. This strong broadband impact feature perfectly matches the theoretical acoustic waveform characteristics of the stick-slip phenomenon, thereby forming conclusive, closed-loop evidence that the larger layer thickness induces severe stick-slip behavior, which consequently leads to a dramatic escalation in friction-induced noise.

To further reveal the relationship between the CoF and friction noise, we plotted the time-domain evolution of the CoF within the 19 to 21 s interval. To better illustrate the variation trend of the average friction force, a smoothing filter was applied to the curves, as depicted in Fig. 14. As observed from the figure, the average CoF values for the 0.1 mm and 0.2 mm layer thicknesses are comparable, whereas the CoF for the 0.3 mm specimen exhibits a significant increase. Concurrently, the fluctuation amplitude of the CoF for the 0.1 mm specimen is relatively minor, while the 0.2 mm and 0.3 mm specimens display pronounced CoF fluctuations.

Correlating this with the acoustic data in Fig. 14, it becomes evident that despite the 0.1 mm and 0.2 mm specimens having nearly identical average CoF values, the noise amplitude of the 0.2 mm specimen is substantially higher than that of the 0.1 mm specimen (and more comparable to the 0.3 mm specimen), while the 0.3 mm specimen exhibits both the highest CoF and the largest noise amplitude. This demonstrates that the amplitude of friction noise in the experiment is directly correlated with the dynamic fluctuation of the CoF rather than its absolute average magnitude. This finding perfectly aligns with the underlying physical mechanism of the stick-slip phenomenon. It further substantiates our previous arguments, confirming that as the layer thickness increases, periodic stick-slip behavior gradually replaces steady-state continuous sliding to become the dominant friction mechanism.

4. Modelling and validation

Individual regression models were developed to forecast the coefficient of friction and the RMS sound pressure associated with friction-induced noise across different printing parameter settings. Based on the experimental observations, layer thickness, surface printing speed, and extrusion width were treated as independent factors, while the measured CoF and RMS sound pressure served as dependent outputs. Preliminary data exploration revealed nonlinear dependencies among the variables; hence, second-order polynomial models were adopted to capture curvature and potential interaction effects. Model parameters were estimated through least-squares regression using MATLAB, and the performance of each model was assessed based on the coefficient of determination (R^2) and the root mean square error (RMSE). The resulting analytical expressions provide quantitative descriptions of how FDM process parameters influence both frictional and acoustic performance, enabling prediction and optimisation beyond the discrete experimental points.

The quadratic model for coefficient of friction is expressed in Eq. (6).

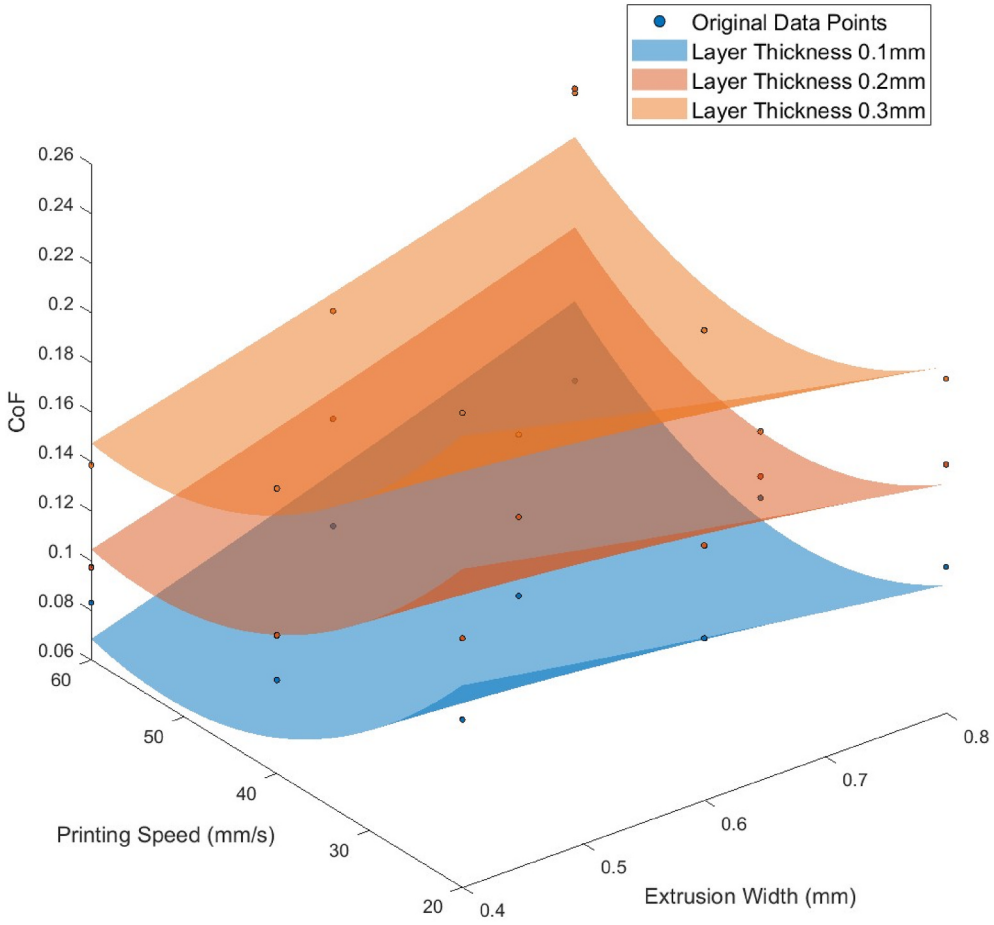


Fig. 15. Fitted response surfaces illustrating the effect of printing speed and extrusion width on the CoF of the Plain surface at different layer thickness levels (0.1, 0.2, and 0.3 mm). The markers represent the original experimental data points.

$$CoF = 0.30366 + 0.48633H - 0.010056V - 0.20989W - 0.0027313H{\cdot}V - 0.15676H{\cdot}W + 0.0059831V{\cdot}W + 0.3355H^2 + 7.6403 \times 10^{-5}V^2 + 0.02614W^2 \quad \text{(Eq.6)}$$

Here, H, V, and W represent layer thickness, printing speed, and extrusion width, respectively. The resulting model demonstrated strong performance, with an R^2 value of 0.826 and an RMSE of 9.67×10^{-4}, indicating its reliability and precision in prediction. Fig. 15 depicts the response surfaces at layer thicknesses of 0.1, 0.2, and 0.3 mm, illustrating smooth and continuous trends throughout the parameter space that closely correspond to the experimental data.

Similarly, the quadratic model for root mean square of sound pressure is formulated as:

$$RMS\ Sound\ Pressure = 4.3996 - 8.747H - 0.032612V + 1.5877W + 0.022810H{\cdot}V + 1.8566H{\cdot}W + 0.0050375V{\cdot}W + 29.409H^2 + 3.8931 \times 10^{-4}V^2 - 1.6277W^2 \quad (7)$$

The model demonstrated a high level of accuracy, achieving an R^2 of 0.932 and an RMSE of 0.0594, which reflects a strong agreement between the predicted values and the observed data. The reported goodness of fit values should be interpreted as indicators of empirical fitting quality within the tested parameter domain, since the input space is limited to three process parameters and the acoustic response is represented by RMS sound pressure as a scalar descriptor. The resulting response surfaces, shown in Fig. 16, reproduce the experimental trends faithfully, with increasing noise amplitude at larger layer heights and relatively minor effects of speed and width. The relatively high R^2 indicate that the models reproduce the observed trends and provide useful interpolation within the tested parameter space. However, they should not be interpreted as evidence that all physical mechanisms governing friction and acoustic response are fully captured.

The quantitative models reinforce the mechanistic insights established earlier. The large positive coefficient associated with layer thickness in both regressions confirms its dominant role in controlling surface roughness and interfacial stability. The small or statistically insignificant coefficients of the cross terms (HV, HW, VW) indicate that printing speed and extrusion width exert only secondary influence and interact weakly with each other. The higher-order terms in layer thickness capture the nonlinear amplification of friction and noise as the printed surface becomes geometrically rougher and mechanically less cohesive. These results demonstrate that, even within a moderate parameter window, the acoustic and frictional responses of FDM-printed PLA are primarily governed by a single process variable, layer thickness, while the remaining parameters serve mainly to fine-tune deposition uniformity.

To further verify predictive performance under unseen parameter combinations, six additional experiments were conducted using the validation matrix listed in Table 6, covering representative combinations of the three printing parameters. The corresponding response surfaces are presented in Fig. 17, where the data from the validation tests align closely with the model predictions for both CoF and RMS sound pressure.

Fig. 17a and b displays the comparison of model outputs against experimental measurements. Regarding the coefficient of friction (CoF), the maximum difference observed from the experimental data is

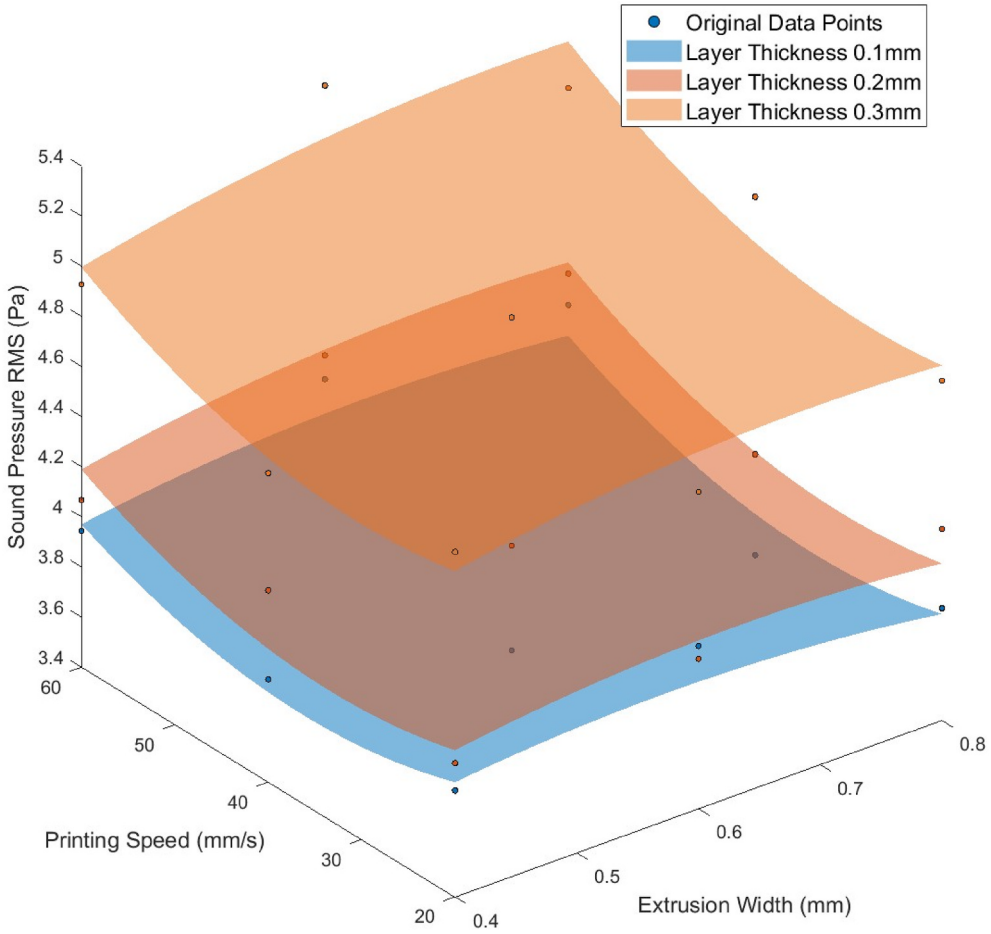


Fig. 16. Fitted response surfaces illustrating the effect of printing speed and extrusion width on the RMS sound pressure of the Plain surface at different layer thickness levels (0.1, 0.2, and 0.3 mm). The markers represent the original experimental data points.

Table 6
Printing parameters of validation experiments.

	Layer Thickness (mm)	Printing Speed (mm/s)	Extrusion Width (mm)
1	0.15	30	0.5
2	0.15	30	0.7
3	0.15	50	0.5
4	0.25	30	0.5
5	0.25	30	0.7
6	0.25	50	0.5

−12.76%, with an average error of 7.40%. In the case of RMS sound pressure, the highest observed error is 10.54%, and the mean error stands at 7.43%. As both average errors are within a 10% margin, the developed quadratic models are demonstrated to be practically accurate and reliable.

5. Conclusion

This research examined how designed surface textures and FDM printing parameters—specifically layer thickness, printing speed at the surface, and extrusion width—affect the frictional performance and noise generation of PLA during dry sliding. The results show that engineered textures do not inherently reduce friction or noise, while layer thickness has the strongest and statistically significant effect on both responses. Printing speed and extrusion width have negligible main effects within the tested range, and only a weak speed–width interaction was observed for CoF.

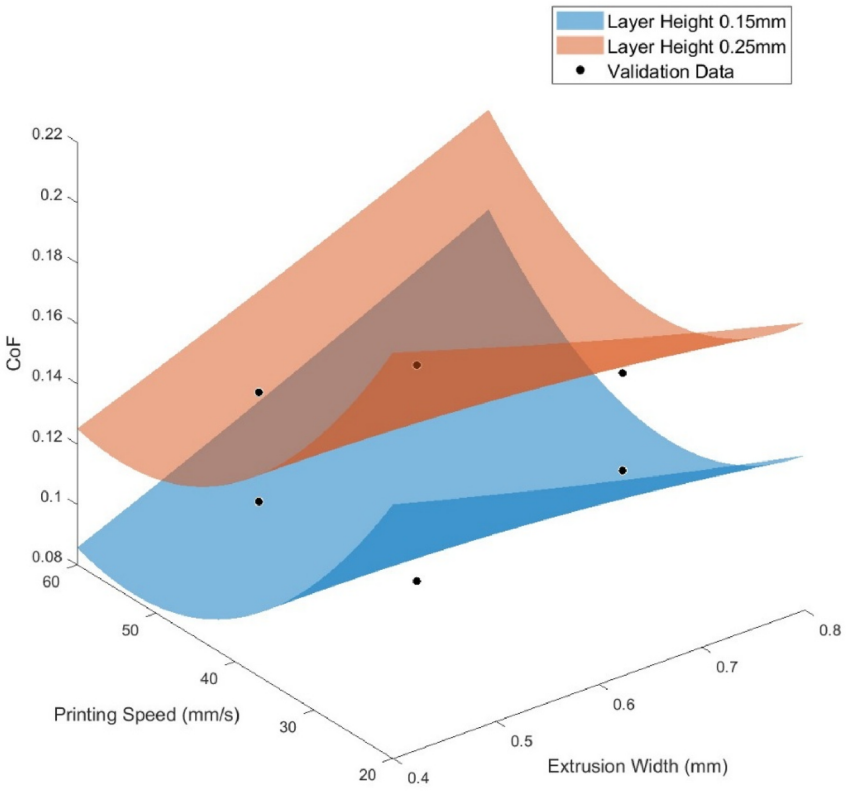
Increasing layer thickness produces a rougher and more compliant top surface, intensifying asperity interaction and stick–slip instability, which elevates both CoF and RMS sound pressure. Thinner layers, in contrast, yield smoother and stiffer surfaces that stabilise sliding and suppress friction-induced vibration.

Two validated quadratic regression models were developed for predicting CoF ($R^2 = 0.826$, RMSE $= 9.67 \times 10^{-4}$) and RMS sound pressure ($R^2 = 0.932$, RMSE $= 0.0594$), with validation experiments showing average prediction errors below 10%, providing practical tools for parameter optimisation. Future studies will focus on detailed surface morphology characterization and extending the investigation to other 3D-printed polymers to further clarify the underlying mechanisms.

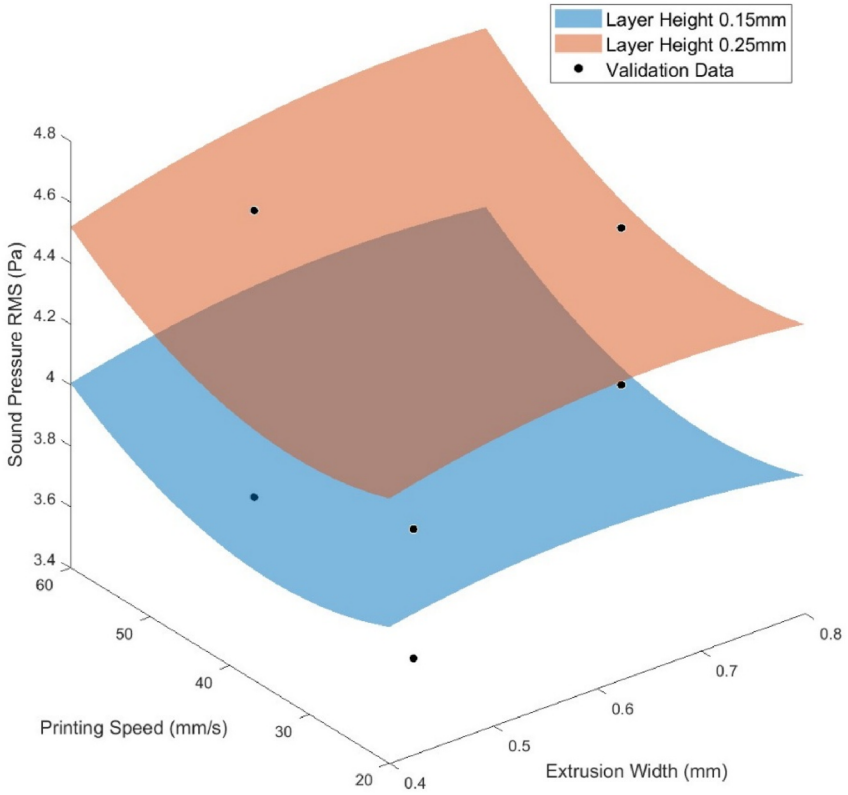
Despite the useful findings and practical predictive capability obtained in this study, several limitations should be acknowledged. The experiments were limited to PLA fabricated by FDM, which restricts the generality of the conclusions. The response surface models are empirical surrogate models for interpolation within the tested parameter domain rather than first-principles physical models. In addition, direct micro-scale characterization of surface morphology and interfacial bonding was not performed, so the proposed mechanism remains an interpretation supported indirectly by signal-level analysis and prior literature. These issues should be addressed in future work.

CRediT authorship contribution statement

Kunbo Lei: Data curation, Formal analysis, Investigation, Methodology, Validation, Visualization, Writing – original draft, Writing – review & editing. **Feiyang He:** Conceptualization, Data curation,



(a)



(b)

Fig. 17. Predicted response surfaces showing the effect of printing speed and extrusion width on the (a) CoF and (b) RMS sound pressure for two layer heights (0.15 mm and 0.25 mm). The black dots represent the experimental validation data used to assess the model accuracy.

Methodology, Project administration, Supervision, Visualization, Writing – original draft, Writing – review & editing. **Muhammad Khan:** Conceptualization, Funding acquisition, Methodology, Project administration, Resources, Software.

Declaration of competing interest

The authors declare that they have no known competing financial interests or personal relationships that could have appeared to influence the work reported in this paper.

Data availability

The dataset supporting this article is publicly available at DOI: 10.17632/hv8rn24nz4.1.

References

[1] N.M. Kinkaid, O.M. O'Reilly, P. Papadopoulos, Automotive disc brake squeal, J. Sound Vib. 267 (1) (2003) 105–166, https://doi.org/10.1016/S0022-460X(02)01573-0.

[2] F.L. Litvin, A. Fuentes, K. Hayasaka, Design, manufacture, stress analysis, and experimental tests of low-noise high endurance spiral bevel gears, Mech. Mach. Theor. 41 (1) (2006) 83–118, https://doi.org/10.1016/j.mechmachtheory.2005.03.001.

[3] N. Tandon, A. Choudhury, A review of vibration and Acoustic measurement methods for the detection of defects in rolling element bearings, Tribol. Int. 32 (8) (1999) 469–480, https://doi.org/10.1016/S0301-679X(99)00077-8.

[4] H. Wei, G. Chen, J. Huang, Z. Chen, Critical review on application of surface texture technology: vibrations and noises reduction, Proc. IME J. J. Eng. Tribol. (2025) 13506501251339103, https://doi.org/10.1177/13506501251339103.

[5] A. Cano-Vicent, M.M. Tambuwala, Sk S. Hassan, D. Barh, A.A.A. Aljabali, M. Birkett, A. Arjunan, Á. Serrano-Aroca, Fused deposition modelling: current status, methodology, applications and future prospects, Addit. Manuf. 47 (2021) 102378, https://doi.org/10.1016/j.addma.2021.102378.

[6] F. He, M. Khan, S. Aldosari, Interdependencies between dynamic response and crack growth in a 3D-Printed Acrylonitrile Butadiene Styrene (ABS) cantilever beam under thermo-mechanical loads, Polymers 14 (5) (2022) 982, https://doi.org/10.3390/polym14050982.

[7] F. He, H. Ning, M. Khan, Effect of 3D printing process parameters on damping characteristic of cantilever beams fabricated using material extrusion, Polymers 15 (2) (2023) 257, https://doi.org/10.3390/polym15020257.

[8] Y. Tian, M. Khan, H. Deng, I. Omar, Quantifying the interrelationship between friction, wear, and noise: a comparative Study on aluminum, brass, and steel, Tribol. Int. 203 (2025) 110403, https://doi.org/10.1016/j.triboint.2024.110403.

[9] P. Papandrea, E. Frigieri, P. Maia, Surface roughness diagnosis in hard turning using acoustic signals and support vector machine: a PCA-based approach, Appl. Acoust. 159 (2020 2020) 107102.

[10] A. Akay, Acoustics of friction, J. Acoust. Soc. Am. 111 (2002) 1525–1548.

[11] S. Pandey, M. Amarnath, Experimental investigations to analyze surface contact fatigue wear by using a dynamic response of the roller bearing system, Int. J. Syst. Assur. Eng. Manag. 14 (2023) 930–949.

[12] Z. Zhang, Z. Zhang, X. Huang, Stability, and transient dynamics of a propeller-shaft system as induced by non-linear friction acting on bearing-shaft contact interface, J. Sound Vib. 333 (2014) 2608–2630.

[13] S.P. Harisubramanyabalaji, C.A. Sribalaji, A. Vivek, G. Vigneshwaran, S. Abhishek, R. Balamurugan, R. Panneer, Development of a theoretical model for prediction of surface roughness of metallic surfaces using acoustic signals, Indian J. Sci. Technol. 8 (22) (2015), https://doi.org/10.17485/ijst/2015/v8i22/79196.

[14] M.M. Hanon, L. Zsidai, Comprehending the role of process parameters and filament color on the structure and tribological performance of 3D printed PLA, J. Mater. Res. Technol. 15 (2021) 647–660, https://doi.org/10.1016/j.jmrt.2021.08.061.

[15] G. Mitaľ, I. Gajdoš, E. Spišák, J. Majerníková, T. Jezný, An analysis of selected technological parameters' influences on the tribological properties of products manufactured using the FFF technique, Appl. Sci. 12 (8) (2022) 3853, https://doi.org/10.3390/app12083853.

[16] F. He, C. Xu, M. Khan, Tribological characterisation and modelling for the fused deposition modelling of polymeric structures under lubrication conditions, Polymers 15 (20) (2023) 4112, https://doi.org/10.3390/polym15204112.

[17] A.I. Portoacă, R.G. Ripeanu, A. Diniță, M. Tănase, Optimization of 3D printing parameters for enhanced surface quality and wear resistance, Polymers 15 (16) (2023) 3419, https://doi.org/10.3390/polym15163419.

[18] V. Mourya, S.P. Bhore, P.G. Wandale, Multiobjective optimization of tribological characteristics of 3D printed texture surfaces for ABS and PLA polymers, J. Thermoplast. Compos. Mater. 37 (2) (2024) 772–799, https://doi.org/10.1177/08927057231185710.

[19] S. Mahmood, E. Guo, A. Stirling, K.D. Schulze, Orientation controls tribological performance of 3D-Printed PLA and ABS, Tribol. Online 18 (6) (2023) 302–312, https://doi.org/10.2474/trol.18.302.

[20] K.R. Hossain, Y. Lyu, X. Yao, Y. Yang, P. Jiang, X. Wang, Tribological and mechanical properties of fabricated soft materials with a podium mesostructured, Tribol. Int. 187 (2023) 108673, https://doi.org/10.1016/j.triboint.2023.108673.

[21] S.K. Prajapati, R. Gnanamoorthy, Surface design of 3D-Printed polyether ether ketone for abrasive wear resistance, Tribol. Trans. 67 (2) (2024) 235–246, https://doi.org/10.1080/10402004.2024.2309903.

[22] L. Bohun, D. Mierzwiński, T. Tepla, S. Gądek, M. Nykiel, A.-M. Vasylieva, Tribological properties of PLA-based composites produced by 3D printing, J. Achievements in Mater. Manufacturing Eng. 128 (1) (2025) 5–17, https://doi.org/10.5604/01.3001.0055.0340.

[23] D. Pieniak, R. Michalczewski, M. Firlej, Z. Krzysiak, K. Przystupa, M. Kalbarczyk, E. Osuch-Słomka, A. Snarski-Adamski, L. Gil, M. Seykorova, Surface layer performance of low-cost 3D-Printed sliding components in metal-polymer friction, Production Engineering Archives 30 (3) (2024) 361–376, https://doi.org/10.30657/pea.2024.30.36.

[24] N. Dhakal, X. Wang, C. Espejo, A. Morina, N. Emami, Impact of processing defects on microstructure, surface quality, and tribological performance in 3D printed polymers, J. Mater. Res. Technol. 23 (2023) 1252–1272, https://doi.org/10.1016/j.jmrt.2023.01.086.

[25] Y. Holovenko, M. Antonov, L. Kollo, I. Hussainova, Friction studies of metal surfaces with various 3D printed patterns tested in dry sliding conditions, Proc. IME J. J. Eng. Tribol. 232 (1) (2018) 43–53, https://doi.org/10.1177/1350650117738920.

[26] M. Wang, X. Wang, J. Liu, J. Wei, Z. Shen, Y. Wang, 3-Dimensional ink printing of friction-reducing surface textures from copper nanoparticles, Surf. Coating. Technol. 364 (2019) 57–62, https://doi.org/10.1016/j.surfcoat.2019.02.080.

[27] H. Yin, W. Chen, D. Xia, H. Wu, P. Jing, L. Chen, L. Zhang, Y. Wang, Z. Wang, D. Li, Friction properties of graphite coating deposited on wedge-shaped textured aluminum alloys prepared by 3D printing, J. Mater. Res. Technol. 20 (2022) 4452–4472, https://doi.org/10.1016/j.jmrt.2022.08.168.

[28] Y. Liu, H. Zhang, S. Dai, G. Dong, Designing a bioinspired scaly textured surface for improving the tribological behaviors of starved lubrication, Tribol. Int. 173 (2022) 107594, https://doi.org/10.1016/j.triboint.2022.107594.

[29] Y. Zhao, L. Yang, Y. Liu, Y. Li, G. Xie, P. Chang, H. Mei, L. Cheng, L. Zhang, Internal and external MoS2/GO heterostructure enhanced multi-point contact egg-box inspired SiOC for macroscopic ultra-low friction, Carbon 221 (2024) 118908, https://doi.org/10.1016/j.carbon.2024.118908.

[30] S. Guo, W. Chen, H. Wang, Z. Qiu, B. Wei, J. Cheng, H. Yuan, Y. Zhou, H. Luo, Simulation and experimental research on the cavitation phenomenon of wedge-shaped triangular texture on the surface of 3D-Printed titanium alloy materials, Tribol. Int. 198 (2024) 109869, https://doi.org/10.1016/j.triboint.2024.109869.

[31] Z. Wang, Y. Liu, B. Jiang, Z. Xin, Z. Jiao, Three-dimensional-printed biomimetic structural ceramics with excellent tribological properties, Materials 18 (6) (2025) 1376, https://doi.org/10.3390/ma18061376.

[32] M. Afshar-Mohajer, X. Yang, R. Long, M. Zou, 3D printing of Micro/nano-hierarchical structures with various structural stiffness for controlling friction and deformation, Addit. Manuf. 62 (2023) 103368, https://doi.org/10.1016/j.addma.2022.103368.

[33] W. Yuan, Y. Yao, L. Keer, Y. Jiao, J. Yu, Q. Li, X.-Q. Feng, 3D-Printed biomimetic surface structures with abnormal friction properties, Extreme Mech. Lett. 26 (2019) 46–52, https://doi.org/10.1016/j.eml.2018.12.003.

[34] M. Luo, Q. He, H. Wang, L. Chang, Tribological behavior of surface textured short carbon fiber-reinforced nylon composites fabricated by three-dimensional printing techniques, J. Tribol. 143 (5) (2021) 051105, https://doi.org/10.1115/1.4050372.

[35] K. Gkougkousi, A.E. Karantzalis, P.G. Nikolakopoulos, K.G. Dassios, Synergistic effect of carbon Micro/nano-fillers and surface patterning on the superlubric performance of 3D-Printed structures, Materials 17 (5) (2024) 1215, https://doi.org/10.3390/ma17051215.

[36] M. Cheng, Z. Zhu, B. Wu, L. Ye, K. Song, Simulation and experimental study of the suppression of low-frequency flow noise signals by a placoid-scale skin, Appl. Sci. 14 (9) (2024) 3855, https://doi.org/10.3390/app14093855.

[37] X. Zhang, H. Qi, W. Lin, X. Gu, R. Liu, G. Zhang, Y. Zhang, J. Yu, G. Zhao, RTV coating on 3D printing bionic structure surface with controllable friction and ice adhesion, Colloids Surf. A Physicochem. Eng. Asp. 704 (2025) 135480, https://doi.org/10.1016/j.colsurfa.2024.135480.

[38] C. Li, X. Gu, H. Xiong, H. Qi, J. Yu, L. Guo, X. Yi, K. Li, Research on strategies for enhancing ice-phobic properties of elastic coatings based on interfacial stress distribution, Colloids Surf. A Physicochem. Eng. Asp. 710 (2025) 136210, https://doi.org/10.1016/j.colsurfa.2025.136210.

[39] S. Yuan, N. Lin, W. Wang, H. Zhang, Z. Liu, Y. Yu, Q. Zeng, Y. Wu, Correlation between surface textural parameter and tribological behaviour of four metal materials with laser surface texturing (LST), Appl. Surf. Sci. 583 (2022) 152410, https://doi.org/10.1016/j.apsusc.2021.152410.

[40] X. Chen, Y. Wang, X. Zhu, W. Sheng, L.Y. Chan, Design and construction of high-performance surface textures for precast concrete pavements: a flexible formwork and 3D printing assisted texturing method, Case Stud. Constr. Mater. 22 (2025) e04576, https://doi.org/10.1016/j.cscm.2025.e04576.

[41] G. Lu, W. Lu, X. Shi, J. Zhang, Z. Yang, W. Chen, Effects of Ni3Al matrix bio-inspired shell-like composite surface structure on interfacial tribological behaviors, Tribol. Int. 170 (2022) 107522, https://doi.org/10.1016/j.triboint.2022.107522.

[42] S. Jolivet, S. Mezghani, M. El Mansori, R. Vargiolu, H. Zahouani, Experimental study of the contribution of gear tooth finishing processes to friction noise, Tribol. Int. 115 (2017) 70–77, https://doi.org/10.1016/j.triboint.2017.05.004.

[43] M.M. John, M. Hanief, Frictional noise mitigation using synergetic approach of laser surface texturing and bio-lubrication, Tribol. Int. 178 (2023) 108056, https://doi.org/10.1016/j.triboint.2022.108056.

[44] Department of Mechanical Engineering, Faculty of Engineering, Tarsus University, S.H. Yetgin, Impact of multi-walled carbon nanotube and graphene oxide on abrasive wear performance of polypropylene, Res. Eng. Struct. Mater (2021), https://doi.org/10.17515/resm2020.176na0118.
[45] P.K. Prajapati, S. Kumar, K.K. Singh, Optimization of tribological behavior of CFRP composites under dry sliding condition using taguchi method, Mater. Today Proc. 21 (2020) 1320–1329, https://doi.org/10.1016/j.matpr.2020.01.169.
[46] S. Wang, A. Chen, L. Li, X. Zhang, Tribological and vibrational effects of laser surface texturing on steel-steel sliding contact, J. Phys., Conf. Ser. 1106 (2018) 012020, https://doi.org/10.1088/1742-6596/1106/1/012020.
[47] F. Peng, X. Shi, Y. Xue, Q. Huang, C. Wu, Tribological properties and friction-induced noise performance of M50 with curved microchannels filled by sn-ag-cu and Ti3C2, J. Mater. Eng. Perform. 31 (2) (2022) 1118–1129, https://doi.org/10.1007/s11665-021-06286-y.
[48] B. Zhou, J. Ma, Z. Yang, X. Shi, Noise reduction mechanism and analysis of TC4 with dimple textured surfaces, J. Mater. Eng. Perform. 30 (5) (2021) 3859–3871, https://doi.org/10.1007/s11665-021-05699-z.
[49] B. Ma, W. Lu, L. Yu, C. Xiong, G. Dang, X. Chen, Friction-wear and noise characteristics of friction disks with circular texture, Materials 17 (10) (2024) 2337, https://doi.org/10.3390/ma17102337.
[50] A. Gadelmoula, S.A. Aldahash, Dry friction and wear behavior of laser-sintered graphite/carbon fiber/polyamide 12 composite, Polymers 15 (19) (2023) 3916, https://doi.org/10.3390/polym15193916.
[51] A. Madison, K. Koren, E. Kames, B. Morkos, Examining the effect of friction during dry sliding on select thermoplastics, in: Volume 6: 15Th International Conference on Multibody Systems, Nonlinear Dynamics, and Control, American Society of Mechanical Engineers, Anaheim, California, USA, 2019, https://doi.org/10.1115/DETC2019-98403. V006T09A031.
[52] Y. Lu, D. Han, Q. Fu, X. Lu, Y. Zhang, Z. Wei, Y. Chen, Experimental investigation of stick-slip behaviors in dry sliding friction, Tribol. Int. 201 (2025) 110221, https://doi.org/10.1016/j.triboint.2024.110221.
[53] J. Zhang, C. Wu, X. Shi, Y. Xue, Q. Huang, K. Zhang, Tribological properties and frictional noise behavior of inconel 625 with micro-texture filled by sn-ag-cu, J. Mater. Eng. Perform. 31 (1) (2022) 82–93, https://doi.org/10.1007/s11665-021-06157-6.
[54] C. Guangxiong, Z. Zhongrong, P. Kapsa, L. Vincent, Effect of surface topography on formation of squeal under reciprocating sliding, Wear 253 (3–4) (2002) 411–423, https://doi.org/10.1016/S0043-1648(02)00161-8.



https://dspace.org/

Tribo-acoustic informatics of FDM printed PLA surfaces under dry sliding: the coupled influence of printing parameters and surface structures

Lei, Kunbo; He, Feiyang; Khan, Muhammad A.

2026-08-15
Elsevier
https://doi.org/10.1016/j.wear.2026.206758
Lei K, He F, Khan M. (2026) Tribo-acoustic informatics of FDM printed PLA surfaces under dry sliding: the coupled influence of printing parameters and surface structures. Wear, Volume 599, August 2026, Article number 206758

Downloaded from a DSpace repository. https://dspace.org/